Journal of Scientific Computing (2021) 88:24
https://doi.org/10.1007/s10915-021-01540-w

Unfitted Nitsche's Method for Computing Wave Modes in Topological Materials

Hailong Guo[1] · Xu Yang[2] · Yi Zhu[3]

Received: 21 September 2020 / Revised: 21 April 2021 / Accepted: 26 May 2021 / Published online: 8 June 2021

Abstract
In this paper, we propose an unfitted Nitsche's method for computing wave modes in topological materials. The proposed method is based on the Nitsche's technique to study the performance-enhanced topological materials which have strongly heterogeneous structures (e.g., the refractive index is piecewise constant with high contrasts). For periodic bulk materials, we use Floquet-Bloch theory and solve an eigenvalue problem on a torus with unfitted meshes. For the materials with a line defect, a sufficiently large domain with zero boundary conditions is used to compute the localized eigenfunctions corresponding to the edge modes. The interfaces are handled by the Nitsche's method on an unfitted uniform mesh. We prove the proposed methods converge optimally. Several numerical examples are presented to validate the theoretical results and demonstrate the capability of simulating topological materials.

Keywords Nitsche's method · Photonic graphene · Topological material · Edge state

1 Introduction

The past decade has witnessed an explosion of research on topological materials. The delicate structures of these materials admit novel and subtle propagating wave patterns which are immune to backscattering from disorder and defects [2,23,31,36,37]. The underlying mechanism is the existence of so-called "topologically protected edge states". These wave modes, which propagate along and decay rapidly transverse to the edge, are robust against

✉ Yi Zhu
yizhu@tsinghua.edu.cn

Hailong Guo
hailong.guo@unimelb.edu.au

Xu Yang
xuyang@math.ucsb.edu

[1] School of Mathematics and Statistics, The University of Melbourne, Parkville, VIC 3010, Australia

[2] Department of Mathematics, University of California, Santa Barbara, CA 93106, USA

[3] Yau Mathematical Sciences Center and Department of Mathematical Sciences, Tsinghua University, Beijing 100084, People's Republic of China

local defects. Thus they are excellent carriers for transferring energy, information and so on . Over the past few years, in addition to the electronic system in which the topological phenomena was firstly studied, such topological phenomena have been experimentally realized in many other physical systems, such as electromagnetic waves in photonic systems and acoustic waves in phononic systems [1,3,31,32,39,42,43].

There are many physical models which admit topologically protected edge states. This work is concerned with wave modes in topological photonic materials. The mathematical problem that we study is the following eigenvalue problem

$$\mathcal{L}^W \Psi \equiv -\nabla \cdot W(\mathbf{x}) \nabla \Psi(\mathbf{x}) = E\Psi(\mathbf{x}), \quad \mathbf{x} = (x_1, x_2) \in \mathbb{R}^2. \tag{1.1}$$

This equation can arise in the in-plane propagation of electromagnetic waves in a photonic crystal whose permittivity is invariant along the longitudinal direction. In this scenario, the electromagnetic fields $(E_1, E_2, E_3, H_1, H_2, H_3)$ can be divided into two decoupled components: transverse electric (TE) mode (E_1, E_2, H_3) and transverse magnetic (TM) mode (H_1, H_2, E_3). The admissible TE modes in a specific material, characterized by the material weight function $W(\mathbf{x})$, satisfy the above eigenvalue problem (1.1). Here, $\Psi(\mathbf{x})$ corresponds to the longitudinal magnetic field H_3 and the eigenvalue E equals ω^2 with ω being the frequency of the electromagnetic fields. The other two components of the TE modes are $(E_1, E_2) = \pm\frac{i}{\sqrt{E}}\left(-\partial_{x_2}\Psi, \partial_{x_1}\Psi\right)$ corresponding to frequency $\pm\sqrt{E}$ respectively. We refer to [21,24] for more details. Though the eigenvalue problem (1.1) can also be obtained in other physical systems such as acoustic waves, we restrict our physical applications in the photonic aspect.

To ensure the existence of topological edge states, specific structures are required for the material weight $W(\mathbf{x})$. Here we focus on the honeycomb-based material weight. The corresponding material is referred to as "photonic graphene". Specifically, the material weight is of the form

$$W(\mathbf{x}) = A(\mathbf{x}) + \delta\kappa(\delta\mathbf{k}_2 \cdot \mathbf{x})B(\mathbf{x}), \tag{1.2}$$

where $A(\mathbf{x})$ and $B(\mathbf{x})$ are hexagonally periodic Hermitian matrices, $\kappa(\cdot) \in \mathbb{R}$ is a bounded transition function, $\delta > 0$ is a parameter characterizing the intensity and width of the transition, and the detailed conditions are given in Sect. 2. From the application point of view, we need to obtain the bulk property (i.e., $\delta = 0$) and edge state property. Understanding the bulk property requires that we solve the eigenvalue problem on a torus using the Floquet-Bloch theory. A topological material can be constructed by gluing two bulks together by the transition function. Consequently, to investigate the wave modes in topological materials, we have to solve the eigenvalue problem on a cylinder since the existence of the transition breaks the periodicity along one direction.

Regarding the analytical understanding of the eigenvalue problem (1.1) with the material weight (1.2), Lee-Thorp et al. proved that the perfect honeycomb material weight ensures the existence of Dirac points in the spectrum, which can be used to construct topological edge states [24]. They also perturbatively constructed the edge states for specific parallel wavenumbers when δ is small and the material weight $W(\mathbf{x})$ is smooth. Their work greatly extends our knowledge on the understanding of topological edge states in a photonic system. However, their results are mostly on the existence aspect and lack the global structure of the bulk dispersion relation and edge states. All of these important studies rely on numerical simulations.

Due to the particular structure of the photonic crystals, spectral method and finite element method are the two most popular methods. The spectral method utilizes the periodicity

of the coefficients and eigenfunctions. Expanding the coefficients and Bloch modes into Fourier series and truncating the series into finite terms, the spectral method can achieve an exponential accuracy for smooth material weight $W(\mathbf{x})$. It is widely used for computing Bloch modes and corresponding energy surfaces [38,41]. However, one of the main shortcomings is that the final matrix is usually not sparse. If the material weight varies drastically or contain discontinuities which is the scenario of this paper, this method requires a large number of Fourier modes to resolve the coefficients. Thus the computation becomes expensive to solve the numerical algebra associated with a large and dense matrix. Actually, our numerical examples show that Fourier spectral method can lead to unreliable and even wrong results when the contrast (jump ratio) of the material weight is very high (see Fig. 6).

A competitive alternative is the finite element method. In fact, finite element methods have been adopted in the computation of topological edge modes. In our recent work [16], we proposed a superconvergent post-processing method to compute topological edge modes for photonic graphene with smooth weight coefficient. The key idea is to recover more accurate gradients for numerical eigenfunctions and use them to improve the accuracy of approximate eigenvalues by using the Rayleigh quotient. The superconvergent recovered gradient also enables us to reconstruct the full electromagnetic fields in real applications. Due to the high contrast nature of the material coefficient, the proposed method can not be generalized directly. The main difficulties are caused by the heterogeneous structure. The existence of the jump in the material weight W implies the non-smoothness of eigenfunctions across the material interfaces. Although the classical finite element methods will work if the underlying mesh is fitted to the interface [5,9,13], it is in general time-consuming and nontrivial to generate a body-fitted mesh. The drawbacks become more serious for the interface with complicated geometric structure. For the honeycomb structure, the discontinuities in the material weight function is copied periodically, which makes the generation of body-fitted meshes become challenging. Furthermore, the unstructured nature of the body-fitted meshes will introduce additional difficulties to impose the periodic or Bloch periodic boundary condition. Those difficulties can be alleviated by adopting the unfitted numerical methods where the underlying meshes are independent of the location of the material interface. To handle the non-smoothness across the material over the interface, one may need modify the finite difference stencil [25,27,34,35], finite element basis functions [12,15,19,20,26,28,29], or the weak formulation [4,8,14,18].

The main purpose of the paper is to propose a new kind of unfitted Nitsche's method based on the Floquet-Bloch transformation for computing the dispersion relation and wave modes in a honeycomb structure with strong heterogeneities. The unfitted Nitsche's method was originally proposed in [18] for the elliptic interface problem with real coefficients. The key idea is to construct the approximation on each fictitious domain induced by the material interface and couple them together by the Nitsche's technique [33]. For the development and application of the unfitted Nitsche's method, the interesting readers are referred to the recent review paper [8]. Compared to the existing unfitted Nitsche's methods [4,8,18], the proposed unfitted Nitsche's method uses Floquet-Bloch theory and solves an eigenvalue problem on a torus. For the $\mathcal{C}$-symmetry breaking case where the eigenvalue problem contains complex matrix-valued coefficients, we use a sufficiently large domain with zero boundary conditions to compute the localized eigenfunctions (edge mode).

One of the difficulties in analyzing the stability of the discrete Nitsche's bilinear form is that it involves the solution itself in addition to its gradient. To the best of our knowledge, the existing unfitted Nitsche's method only focuses on the pure diffusion equation. To establish the stability, we need the trace theorem on cut elements, i.e. elements cut by the interface. The existing trace theorem [8,18] for the cut element involves both parts of the cut element. Direct

application of the theorem is not able to entitle us the full possibility to prove the coercivity of the Nitsche's bilinear form. Therefore, we build up a new trace inequality which involves only one part of the cut element. The new trace inequality enables us to establish the stability and continuity for Nitsche's bilinear form in term of the energy norm. Using the approximation theory of the compact operator [6] and the interpolation error estimates, we are able to show the optimal convergence results for both discrete eigenvalue and eigenfunctions using the proposed unfitted Nitsche's method. In particular, the established error estimates are independent of the location of the interface. Furthermore, we show that there is no pollution in the numerical spectrum.

The rest of the paper is organized as follows. In Sect. 2, we present the physical background of photonic graphene and the mathematical setup. In Sect. 3, we focus on the computation of the dispersion relation and wave modes. We start the section by introducing the formulation of the unfitted Nitsche's method on the torus which gives us the unperturbed bulk properties. The stability and continuity of the unfitted Nitsche's weak formulation are established. Then, we extend the unfitted Nitsche's method to compute wave modes on a cylinder domain which corresponds to the physical setup of topological materials. In Sect. 4, we prove the numerically approximated eigenpairs converge optimally to the exact eigenpairs. In Sect. 5, we present several numerical examples to justify the theoretical results. We make conclusive remarks in Sect. 6.

2 Physical Problems and Preliminaries

We will focus on the honeycomb-based photonic materials, and present the physical setup and briefly review the underlying theory.

2.1 Honeycomb Structured Material Weight

We consider the following specific hexagonal lattice

$$\Lambda = \mathbb{Z}\mathbf{v}_1 + \mathbb{Z}\mathbf{v}_2 = \{m_1\mathbf{v}_1 + m_2\mathbf{v}_2 : m_1,\ m_2 \in \mathbb{Z}\}, \tag{2.1}$$

with the lattice basis vectors

$$\mathbf{v}_1 = \begin{pmatrix} \frac{\sqrt{3}}{2} \\ \\ \frac{1}{2} \end{pmatrix}, \quad \mathbf{v}_2 = \begin{pmatrix} \frac{\sqrt{3}}{2} \\ \\ -\frac{1}{2} \end{pmatrix}.$$

The fundamental cell is chosen to be the parallelogram:

$$\Omega = \{\theta_1\mathbf{v}_1 + \theta_2\mathbf{v}_2 : 0 \le \theta_j \le 1,\ j = 1, 2\}, \tag{2.2}$$

with $|\Omega|$ standing for the area of Ω. The hexagonal lattice and its fundamental cell are illustrated in Fig. 1a. Note that this parallelogram cell is periodically equivalent to one hexagon [2].

The dual lattice

$$\Lambda^* = \{m_1\mathbf{k}_1 + m_2\mathbf{k}_2 := (m_1, m_2) \in \mathbb{Z}^2\} = \mathbb{Z}\mathbf{k}_1 \oplus \mathbb{Z}\mathbf{k}_2, \tag{2.3}$$

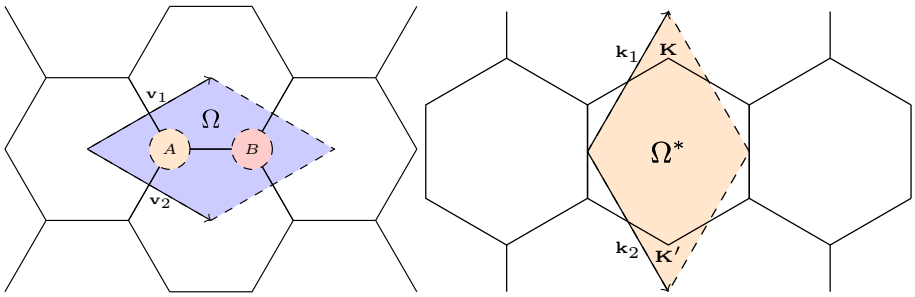

Fig. 1 Two dimensional hexagonal structure. **a** Hexagonal lattice with lattice vector $\mathbf{v}_j$, $j = 1, 2$ and the unit cell Ω with two air holes centered at A and B; **b** Dual hexagonal lattice with the fundamental dual cell Ω^*

is generated by the dual lattice vectors $\mathbf{k}_1$, $\mathbf{k}_2$ which satisfy $\mathbf{k}_i \cdot \mathbf{v}_j = 2\pi\delta_{ij}$, $(i, j = 1, 2)$. Specifically, the dual lattice vectors are

$$\mathbf{k}_1 = \frac{4\sqrt{3}}{3}\begin{pmatrix} \frac{1}{2} \\ \frac{\sqrt{3}}{2} \end{pmatrix}, \quad \mathbf{k}_2 = \frac{4\sqrt{3}}{3}\begin{pmatrix} \frac{1}{2} \\ -\frac{\sqrt{3}}{2} \end{pmatrix}. \tag{2.4}$$

Throughout this work, we choose the parallelogram Ω^*:

$$\Omega^* = \{\theta_1\mathbf{k}_1 + \theta_2\mathbf{k}_2 : -\frac{1}{2} \le \theta_j \le \frac{1}{2}, j = 1, 2\}, \tag{2.5}$$

as the fundamental dual cell. The dual hexagonal lattice and its fundamental dual cell are illustrated in Fig. 1b. In the literature, the fundamental dual cell is often chosen to be the hexagon centered at the origin. This is also referred to as the Brillouin zone of honeycomb lattices [2,11].

Let $\mathbf{A} = \frac{1}{3}(\mathbf{v}_1 + \mathbf{v}_2) \in \Omega$ and $\mathbf{B} = \frac{2}{3}(\mathbf{v}_1 + \mathbf{v}_2) \in \Omega$; see Fig. 1a. Define the honeycomb lattice $\Lambda_h = (\mathbf{A} + \Lambda) \bigcup (\mathbf{B} + \Lambda)$. Note that Λ_h has two sites per unit cell.

Let $B_r(\mathbf{x}_0)$ be the ball centered at $\mathbf{x}_0$ with the radius r. Throughout this work, we require that $r < \frac{1}{2}|\mathbf{A}-\mathbf{B}|$ which implies that $B_r(\mathbf{A})$ and $B_r(\mathbf{B})$ are disjoint. We divide the fundamental cell into two parts, $\Omega_1 = B_r(\mathbf{A}) \bigcup B_r(\mathbf{B})$ and $\Omega_2 = \Omega/\Omega_1$. The interface Γ on the fundamental cell is defined as the intersection of Ω_1 and Ω_2, i.e. $Đ = \partial\Omega_1 \cap \partial\Omega_2$. Define the piece-wise honeycomb function

$$\epsilon(\mathbf{x}) = \begin{cases} \epsilon_{\mathbf{A}}, & \text{if } \mathbf{x} \in B_r(\mathbf{A}) + \Lambda, \\ \epsilon_{\mathbf{B}}, & \text{if } \mathbf{x} \in B_r(\mathbf{B}) + \Lambda, \\ \epsilon_0, & \text{if } \mathbf{x} \in \Omega_2 + \Lambda, \end{cases} \tag{2.6}$$

where ϵ_j, $j = \mathbf{A}, \mathbf{B}, 0$, are positive constants. ϵ_0 is regarded as the value of the background and $\epsilon_{\mathbf{A}}$, $\epsilon_{\mathbf{B}}$ are the values against the background. It is obvious that $\epsilon(\mathbf{x})$ is Λ-periodic, i.e., $\epsilon(\mathbf{x} + \mathbf{v}) = \epsilon(\mathbf{x})$ for all $\mathbf{v} \in \Lambda$.

In this work, we use the following material weight as our prototype

$$W(\mathbf{x}) = \begin{pmatrix} \epsilon(\mathbf{x}) & i\gamma \\ -i\gamma & \epsilon(\mathbf{x}) \end{pmatrix}^{-1}. \tag{2.7}$$

This material weight corresponds to the magneto-optical material [17]. $\gamma \in \mathbb{R}$ is called Farady-rotation constant satisfying $\min(\epsilon(\mathbf{x})^2 - \gamma^2) > c_0 > 0$, which ensures $W(\mathbf{x})$ is

uniformly elliptic. In real materials, the strength of the Faraday-rotation is much smaller than the permitivity ϵ, hence

$$W(\mathbf{x}) \approx \epsilon(\mathbf{x})^{-1} I + \gamma \epsilon^{-2} \sigma_2, \tag{2.8}$$

where $\sigma_2 = \begin{pmatrix} 0 & -i \\ i & 0 \end{pmatrix}$ is a Pauli matrix.

2.2 Eigenvalue Problem on a Torus

Consider the material weight of the form (2.7) or (2.8). $W(\mathbf{x})$ is Λ-periodic when γ is constant. We can restrict our analysis on a torus by Floquet-Bloch theory. Before proceeding further, we introduce the following function space

$$L^2_{per}(\Lambda) = \left\{ f(\mathbf{x}) \in L^2_{loc}\left(\mathbb{R}^2, \mathbb{C}\right) : \ f(\mathbf{x}+\mathbf{v}) = f(\mathbf{x}), \forall \mathbf{v} \in \Lambda, \mathbf{x} \in \mathbb{R}^2 \right\}$$
$$L^2_{\mathbf{k}}(\Lambda) = \left\{ g(\mathbf{x}) : \ e^{-i\mathbf{k}\cdot\mathbf{x}} g(\mathbf{x}) \in L^2_{per}(\Lambda) \right\}.$$

Note that functions in $L^2_{\mathbf{k}}(\Lambda)$ are quasi-periodic. Namely, if $g(\mathbf{x}) \in L^2_{\mathbf{k}}(\Lambda)$, then $g(\mathbf{x}+\mathbf{v}) = e^{i\mathbf{k}\cdot\mathbf{v}} g(\mathbf{x}), \forall \mathbf{v} \in \Lambda$. Similarly, we can also define $H^s_{per}(\Lambda)$ and $H_{\mathbf{k}}(\Lambda)$ in a standard way.

According to Floquet-Bloch theory, the spectrum of $\mathcal{L}^W$ in $L^2(\mathbb{R}^2)$ can be represented by the spectrum $\mathcal{L}^W$ in $L^2_{\mathbf{k}}(\Lambda)$. Namely, we solve the following $L^2_{\mathbf{k}}(\Lambda)$-eigenvalue problem

$$\mathcal{L}^W \Phi(\mathbf{x}) = E\Phi(\mathbf{x}), \qquad \Phi(\mathbf{x}) \in L^2_{\mathbf{k}}(\Lambda). \tag{2.9}$$

Due to the periodicity, we can restrict $\mathbf{k}$ in the fundamental dual cell Ω^*. For a fixed $\mathbf{k} \in \Omega^*$, there exists a sequence of pairs $(E_m(\mathbf{k}), \Phi_m(\mathbf{x}; \mathbf{k}))$, $m = 1, 2, \cdots$ satisfying the above eigenvalue problem. Here $E_m(\mathbf{k})$, $m = 1, 2, \cdots$ are called dispersion band functions which have been ordered as $0 < E_1(\mathbf{k}) \le E_2(\mathbf{k}) \le E_3(\mathbf{k}) \le \cdots$. The corresponding eigenfunctions $\Phi_m(\mathbf{x}; \mathbf{k})$ are referred to as the Bloch waves. Moreover, the set $\{\Phi_m(\mathbf{x}; \mathbf{k}),\ m \in \mathbb{N},\ \mathbf{k} \in \Omega^*\}$ forms a "generalized" basis of $L^2(\mathbb{R}^2)$ and the spectrum of $\mathcal{L}^W$ in $L^2(\mathbb{R}^2)$, $\sigma(\mathcal{L}^W)$, coincides with the Bloch spectrum, the union of the images of all the mappings $E_m(\mathbf{k})$, i.e.,

$$\sigma(\mathcal{L}^W) = \bigcup_{m=1}^{\infty} \left[\inf_{\mathbf{k}\in\Omega^*} E_m(\mathbf{k}), \sup_{\mathbf{k}\in\Omega^*} E_m(\mathbf{k}) \right]. \tag{2.10}$$

In general, it is impossible to solve the eigenvalue problem (2.9) analytically. A natural numerical scheme is the spectral method. Namely, we can expand $W(\mathbf{x})$ and $\Phi(\mathbf{x})$ into their Fourier series. By truncating the series into finite terms, we can easily solve the reduced eigenvalue problem for a matrix. If $W(\mathbf{x})$ is smooth, $\Phi(\mathbf{x})$ is also smooth. We only need a few terms to approximate $W(\mathbf{x})$ and $\Phi(\mathbf{x})$ due to the exponential accuracy. The shortcoming of this method is that the resulting matrix is not sparse. When we need a large number of terms to approximate $W(\mathbf{x})$, this method becomes costly and sometimes lead to wrong results. A typical scenario is that $W(\mathbf{x})$ changes greatly or is even discontinuous and this regime is exactly what we are going to handle.

If $\gamma = 0$, $W(\mathbf{x})$ is a honeycomb structured material defined in [24], i.e., $W(\mathbf{x})$ is even, real and $\frac{2\pi}{3}$-rotation invariant. According to [24], there generically exist the so-called Dirac points—conical singularities in the dispersion band functions $E_m(\mathbf{k})$ at $\mathbf{K} = \frac{1}{3}(\mathbf{k}_1 - \mathbf{k}_2)$, $\mathbf{K}' = -\mathbf{K}$ for some m. If $\gamma \neq 0$ but is still a constant, the material weight $W(\mathbf{x})$ is now complex, local spectral gaps open near the Dirac points due to the complex-conjugate symmetry breaking.

2.3 Honeycomb Structured Material Weight with a Line Defect

Dirac points provide a mechanism to generate the so-called topological edge states via introducing a line defect. Define a transition function (referred to as domain wall function) $\kappa(\zeta) \in L^\infty(\mathbb{R}, \mathbb{R})$ with $\kappa(\pm\infty) = \pm\kappa_\infty$. Without loss of generality, we require that $\kappa_\infty > 0$. A typical example of this transition function is the step function

$$\kappa(\zeta) = \begin{cases} -\kappa_\infty, & \zeta < 0, \\ 0, & \zeta = 0, \\ +\kappa_\infty, & \zeta > 0. \end{cases} \tag{2.11}$$

Its smooth counterpart is $\kappa(\zeta) = \kappa_\infty \tanh(\zeta)$.

A line defect is introduced if we choose the Faraday-rotation γ in (2.7) to be a transition function along a direction. Namely $\gamma = \kappa(\mathbf{n} \cdot \mathbf{x})$ where $\mathbf{n} \neq 0$ is the normal direction of the line defect. Obviously, if $\kappa(\zeta)$ is the step function (2.11), the line $\mathbf{n}^\perp\mathbb{R}$ is the interface of two different materials (we also call it an edge). In this work we take Zigzag edge as our prototype. In this case, $\mathbf{n} = \mathbf{k}_2$ and the line $\mathbf{v}_1\mathbb{R}$ is the edge. Note that $W(\mathbf{x})$ is periodic along $\mathbf{v}_1$ direction but loses the periodicity along $\mathbf{v}_2$ direction.

Let $\Sigma = \mathbb{R}^2/\mathbb{Z}\mathbf{v}_1$ be a cylinder. The fundamental domain for Σ is $\Omega_\Sigma \equiv \{\tau_1\mathbf{v}_1 + \tau_2\mathbf{v}_2 : 0 \le \tau_1 \le 1, \tau_2 \in \mathbb{R}\}$. Define the function spaces

$$L^2_{per}(\Sigma) = \left\{ f(\mathbf{x}) \in L^2(\Omega_\Sigma, \mathbb{C}) : \ f(\mathbf{x} + \mathbf{v}_1) = f(\mathbf{x}) \right\}$$
$$L^2_{k_\parallel}(\Sigma) = \left\{ g(\mathbf{x}) \in L^2(\Omega_\Sigma, \mathbb{C}) : \ g(\mathbf{x} + \mathbf{v}_1) = e^{ik_\parallel} g(\mathbf{x}) \right\}.$$

We solve the eigenvalue problem (1.1) in $L^2_{k_\parallel}(\Sigma)$. Due to the subtle symmetries of the setup, there exists point spectrum with the corresponding eigenfunctions referred as to edge states. Namely, we need to solve the eigenvalue problem

$$\mathcal{L}^W \Psi(\mathbf{x}; k_\parallel) = E(k_\parallel)\Psi(\mathbf{x}; k_\parallel), \tag{2.12}$$
$$\Psi(\mathbf{x} + \mathbf{v}_1; k_\parallel) = e^{\mathrm{i}k_\parallel}\Psi(\mathbf{x}; k_\parallel), \tag{2.13}$$
$$\Psi(\mathbf{x}; k_\parallel) \to 0 \ \text{ as } \ |\mathbf{x} \cdot \mathbf{k}_2| \to \infty.. \tag{2.14}$$

Theoretically, the theory of bulk-boundary correspondence can specify the number of edge states, see for instance [11]. But the global structure of the energy curve of edge states can only be obtained numerically in a generic setup.

3 Unfitted Nitsche's Method

In this section, we propose the Floquet-Bloch theory based unfitted Nitsche's methods for simulating topological materials. We first focus on the computing the bulk dispersion relations. Then, we extend the method to computing edge modes in topological materials. In this paper, we use C, with or without a subscript, to denote a generic constant, which can be different at different occurrences. In addition, it is independent of the mesh size and the location of the interface.

3.1 Unfitted Nitsche's Method for Computing Bulk Dispersion Relation

In this section, we are interested in the efficient numerical solution of the eigenvalue problem (2.9) on a torus. One of the main numerical difficulties is the existence of the high contrast in the material weight $W(\mathbf{x})$, which may lower the regularity of eigenfunctions. To model the discontinuity, we use the interface conditions as [27] and the $L^2_{\mathbf{k}}(\Lambda)$-eigenvalue problem (2.9) can be converted into the following interface $L^2_{\mathbf{k}}(\Lambda)$-eigenvalue problem

$$\mathcal{L}^W \Phi(\mathbf{x}) = E\Phi(\mathbf{x}), \tag{3.1}$$

$$[\![\Psi]\!] = \left[\!\!\left[W\frac{\partial \Psi}{\partial n} \right]\!\!\right] = 0, \quad \text{on } \Gamma; \tag{3.2}$$

where $\Phi(\mathbf{x}) \in L^2_{\mathbf{k}}(\Lambda)$, $[\![v]\!]$ is the jump in value of a function v crossing the interface Γ, and n is the unit outer normal vector of Γ.

To deal with quasi-periodicity of functions in $L^2_{\mathbf{k}}(\Lambda)$, we apply the Floquet-Bloch transform $\Phi(\mathbf{x};\mathbf{k}) = e^{i\mathbf{k}\cdot\mathbf{x}}\phi(\mathbf{x};\mathbf{k})$. We transfer the eigenvalue problem (3.1)–(3.2) to the following interface $L^2_{per}(\Lambda)$-eigenvalue problem

$$\mathcal{L}^W(\mathbf{k})\phi(\mathbf{x}) = E(\mathbf{k})\phi(\mathbf{x}), \tag{3.3}$$

$$[\![\phi]\!] = [\![W(\nabla + i\mathbf{k})\phi \cdot n]\!] = 0, \quad \text{on } \Gamma; \tag{3.4}$$

where $\phi(\mathbf{x}) \in L^2_{per}(\Lambda)$ and

$$\mathcal{L}^W(\mathbf{k}) = (\nabla + i\mathbf{k}) \cdot W(\mathbf{x})(\nabla + i\mathbf{k}). \tag{3.5}$$

To address the numerical challenge brought by the interface condition (3.4), the most straightforward idea is to use finite element methods with body-fitted meshes [5,9] to resolve the discontinuity. However, this brings two new *difficulties*: (1) the body-fitted meshes, in general, are unstructured meshes on which it is difficult to impose the periodic boundary conditions; (2) it is technically hard to generate body-fitted meshes, in particular for topological materials with complicated geometric structures and a huge number of interfaces. In this paper, we avoid those two difficulties by introducing the unfitted Nitsche's methods [8,18].

3.1.1 Unfitted Nitsche's Method on a Torus

This subsection is devoted to the unfitted Nitsche's method for the interface $L^2_{per}(\Lambda)$-eigenvalue problem (3.3)–(3.4). *To avoid the generation of body-fitted meshes for complicated topological structure and simplify the imposing of periodical boundary condition, we partition the fundamental cell Ω using uniform triangular meshes.* The uniform triangulation is obtained by dividing Ω into N^2 sub-rhombuses with mesh size $h = \frac{\|\mathbf{v}_1\|_2}{N}$ and then splitting each sub-rhombs into two isosceles triangles. In addition, we assume that N is sufficiently large such that the following assumption holds:

Assumption 1 The interface Γ intersects each interface element boundary ∂K exactly twice, and each open edge at most once.

The elements of $\mathcal{T}_h$ can be categorized into two different classes: regular elements and interface elements. An element τ is called an interface element if the interface Γ passes

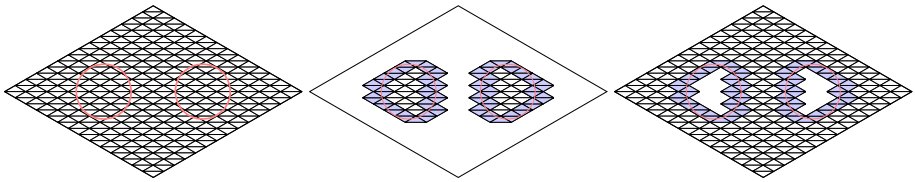

Fig. 2 Illustration of the fictitious domain decomposition of the fundamental cell Ω. **a** Triangulation $\mathcal{T}_h$ of the fundamental cell Ω; **b** Triangulation $\mathcal{T}_{1,h}$ of $\Omega_{1,h}$; **c** Triangulation $\mathcal{T}_{2,h}$ of $\Omega_{2,h}$

through K. The set of all elements that intersect the interface Γ is denoted by $\mathcal{T}_{\Gamma,h}$. Then, we have

$$\mathcal{T}_{\Gamma,h} = \left\{K \in \mathcal{T}_h : \Gamma \cap \overline{K} \neq \emptyset\right\}. \tag{3.6}$$

Denote the union of all such type elements by

$$\Omega_{\Gamma,h} = \bigcup_{K \in \mathcal{T}_{\Gamma,h}} K, \tag{3.7}$$

and the set of all elements covering subdomain Ω_i by

$$\mathcal{T}_{i,h} = \left\{K \in \mathcal{T}_h : \overline{\Omega_i} \cap \overline{K} \neq \emptyset\right\}, \quad i = 1, 2. \tag{3.8}$$

Let

$$\Omega_{i,h} = \bigcup_{K \in \mathcal{T}_{i,h}} K, \quad \omega_{i,h} = \bigcup_{K \in \mathcal{T}_{i,h} \setminus \mathcal{T}_{\Gamma,h}} K, \quad i = 1, 2. \tag{3.9}$$

Figure 2 gives an illustration of $\Omega_{i,h}$ and $\omega_{i,h}$. We remark that $\Omega_{1,h}$ and $\Omega_{2,h}$ overlap on $\Omega_{\Gamma,h}$, which is shown as the blue part in Fig. 2b, c.

One of main ingredients of the unfitted Nitsche's method is to define the finite element space as the direct sum of the standard continuous linear finite element space on $\Omega_{i,h}$. For such a purpose, we let $V_{i,h}$ be the standard continuous linear finite element space on $\Omega_{i,h}$, i.e.

$$V_{i,h} = \left\{v \in C^0(\Omega_{i,h}) : v|_K \in \mathbb{P}_1(K) \text{ for any } K \in \mathcal{T}_{i,h}\right\}, \quad i = 1, 2, \tag{3.10}$$

where $\mathbb{P}_k(K)$ is the space of polynomials with degree less than or equal to k on the element K. The finite element space for the unfitted Nitsche's method is defined as $V_h = V_{1,h} \oplus V_{2,h}$. In other words,

$$V_h = \left\{v_h = (v_{1,h}, v_{2,h}) : v_{i,h} \in V_{i,h},\ i = 1, 2\right\}. \tag{3.11}$$

To impose the periodic boundary condition, we introduce $V_{h,per}$ as a subspace of V_h which is defined as

$$V_{h,per} = \left\{v_h \in V_h : v_h(\mathbf{x} + \mathbf{v}) = v_h(\mathbf{x}), \forall \mathbf{v} \in \Lambda, \mathbf{x} \in \mathbb{R}^2\right\}. \tag{3.12}$$

Note that a function in V_h (or $V_{h,per}$) is a vector-valued function from $\mathbb{R}^2 \mapsto \mathbb{R}^2$, which has a zero component in $\omega_{1,h} \bigcup \omega_{2,h}$ but in general two non-zero components in $\mathcal{T}_{\Gamma,h}$. It means that there are two sets of basis functions for any element K in $\mathcal{T}_{\Gamma,h}$: one for $V_{1,h}$ and the other for $V_{2,h}$.

For any interface element K in $\mathcal{T}_{\Gamma,h}$, let $K_i = K \cap \Omega_i$ be the part of K in Ω_i, where $|K_i|$ is the area of K_i. Similarly, let $\Gamma_K = \Gamma \cap K$ be the part of Γ in K, where $|\Gamma_K|$ is the measure of Γ_K in $\mathbb{R}^1$. Different from the interface elliptic problem considered for unfitted Nitsche's method in [14,18], the material weight coefficient $W(\mathbf{x})$ is complex and matrix-valued. To increase the robustness of the Nitsche's method, we introduce two weights using the maximal norm of W inspired by [4]

$$\kappa_1|_K = \frac{\|W_2\|_\infty |K_1|}{\|W_2\|_\infty |K_1| + \|W_1\|_\infty |K_2|}, \quad \kappa_2|_K = \frac{\|W_1\|_\infty |K_2|}{\|W_2\|_\infty |K_1| + \|W_1\|_\infty |K_2|}, \tag{3.13}$$

which satisfies that $\kappa_1 + \kappa_2 = 1$. In (3.13), $\|W_i\|_\infty$ denotes the maximum of L^∞-norm of each component of W_i in the subdomain Ω_i. Then, we define the weighted averaging of a function v_h on the interface Γ as

$$\{\{v_h\}\} = \kappa_1 v_{1,h} + \kappa_2 v_{2,h}. \tag{3.14}$$

Furthermore, we define the constant λ_K as

$$\lambda_K = \frac{h\|W_1\|_\infty \|W_2\|_\infty |\Gamma_K|}{\|W_2\|_\infty |K_1| + \|W_1\|_\infty |K_2|}. \tag{3.15}$$

Based on λ_K, we define element-wise parameter λ as $\lambda|_K = \hat{\lambda}\lambda_K$ for some large enough positive number $\hat{\lambda}$ (called stabilizing parameter). It is easy to see that $\lambda_K \le \|W\|_\infty := \max(\|W_1\|_\infty, \|W_2\|_\infty)$.

The unfitted Nitsche's method for the interface $L^2_{per}(\Lambda)$-eigenvalue problem (3.3)–(3.4) is to find the the eigenpair $(\phi_h, E_h(\mathbf{k})) \in V_{h,per} \times \mathbb{R}$ with $\phi_h \neq 0$ such that

$$a_h(\phi_h, q_h) = E_h(\mathbf{k}) b(\phi_h, q_h), \quad \forall q_h \in V_{h,per}, \tag{3.16}$$

where

$$\begin{aligned} a_h(\phi_h, q_h) = &\sum_{i=1}^{2} \int_{\Omega_i} W(\nabla + \mathrm{i}\mathbf{k})\phi_h \cdot \overline{(\nabla + \mathrm{i}\mathbf{k})q_h} d\mathbf{x} - \int_\Gamma \{\{W(\nabla + \mathrm{i}\mathbf{k})\phi_h \cdot n\}\}[\![\overline{q_h}]\!] ds \\ &- \int_\Gamma \{\{\overline{W(\nabla + \mathrm{i}\mathbf{k})q_h \cdot n}\}\}[\![\phi_h]\!] ds + \frac{1}{h}\int_\Gamma \lambda [\![\phi_h]\!][\![\overline{q_h}]\!] ds, \end{aligned} \tag{3.17}$$

and

$$b(\phi_h, q_h) = \int_\Omega \phi_h \cdot \overline{q_h} d\mathbf{x}, \tag{3.18}$$

where h is the mesh size. The weak formulation (3.16) is called the Nitsche's weak formulation.

3.1.2 Well-Posedness of the Unfitted Nitsche's Method on a Torus

In this part, we shall show the unfitted Nistche's method is well-posed. We start by showing the following consistency result:

Lemma 1 *Let (ϕ, E) be the eigenpair of the interface $L^2_{per}(\Lambda)$-eigenvalue problem (3.3)–(3.4). Then (ϕ, E) satisfies*

$$a_h(\phi, q) = E(\mathbf{k}) b(\phi, q), \quad \forall q \in H^1_{per}, \tag{3.19}$$

Proof For any $\phi, q \in H^1_{per}$, we notice that $[\![\phi]\!] = [\![q]\!] = 0$ and hence $a_h(\cdot,\cdot)$ is reduced to the standard bilinear formulation. Then (3.19) follows by the Green's formula on each subdomain Ω_i and the interface condition (3.4). □

Let us introduce the following interface $L^2_{per}(\Lambda)$-source problem

$$\mathcal{L}^W(\mathbf{k})u(\mathbf{x}) = f(\mathbf{k}), \tag{3.20}$$

$$[\![u]\!] = [\![W(\nabla + \mathrm{i}\mathbf{k})u \cdot n]\!] = 0, \quad \text{on } \Gamma; \tag{3.21}$$

Thanks to the above Lemma, we can easily deduce following corollary which is known as the Galerkin orthogonality for the source problem:

Corollary 1 *Let u be the solution of the interface problem (3.20)–(3.21) and u_h be the corresponding finite element approximate by the unfitted Nitsche's method. Then we have*

$$a_h(u - u_h, v_h) = 0, \quad \forall v_h \in V_{h,per}. \tag{3.22}$$

To analyze the stability of the bilinear form $a_h(\cdot,\cdot)$, we introduce the following mesh-dependent norm [8,18]

$$|||\phi|||_h^2 = \|(\nabla + \mathrm{i}\mathbf{k})\phi\|^2_{0,\Omega_1\cup\Omega_2} + \sum_{K\in\mathcal{T}_{\Gamma,h}} h^{-1}\|[\![\phi]\!]\|^2_{0,\Gamma_K}. \tag{3.23}$$

We prepare our proof of the stability of the bilinear form by establishing the following Lemma, whose proof is given in Appendix A.

Lemma 2 *Let ϕ_h be a finite element function in V_h. Then the following inequalities hold:*

$$\|\phi_{i,h}\|^2_{0,\Gamma_K} \le C_1 \frac{h^2|\Gamma_K|}{|K_i|}\|\nabla\phi_{i,h}\|^2_{0,K_i}, \tag{3.24}$$

$$\|\nabla\phi_{i,h}\|^2_{0,\Gamma_K} \le C_2 \frac{|\Gamma_K|}{|K_i|}\|\nabla\phi_{i,h}\|^2_{0,K_i}. \tag{3.25}$$

Remark 1 The inequality of (3.24) is a refinement of the trace inequality on a cut element in [18]. It is the key to show the stability of the bilinear form.

Based on the above Lemma, we establish the following error estimates for the weighted averaging.

Lemma 3 *Let q_h be a finite element function in V_h. Then the following inequalities hold:*

$$\|\{\!\{(W\mathbf{k}q)\cdot\mathbf{n}\}\!\}\|^2_{0,\Gamma_K} \le C_3 h\|\mathbf{k}\|^2\lambda_K\|W\|_\infty\|\nabla q_h\|^2_{0,K_1\cup K_2}, \tag{3.26}$$

$$\|\{\!\{(W\nabla q)\cdot\mathbf{n}\}\!\}\|^2_{0,\Gamma_K} \le C_4 h^{-1}\lambda_K\|W\|_\infty\|\nabla q_h\|^2_{0,K_1\cup K_2}. \tag{3.27}$$

Proof Using (3.13) and (3.15), we can deduce from Lemma 2 that

$$\begin{aligned}
&\|\{\!\{W\mathbf{k}q)\cdot\mathbf{n}\}\!\}\|^2_{0,\Gamma_K}\\
&\quad=\|\kappa_1(W_1\mathbf{k}q_{1,h})\cdot\mathbf{n}+\kappa_2(W_2\mathbf{k}q_{2,h})\cdot\mathbf{n})\|^2_{0,\Gamma_K}\\
&\quad\le 2\kappa_1^2\|\mathbf{k}\|^2\|W_1\|^2_\infty\|q_{1,h}\|^2_{0,\Gamma_K}+2\kappa_2^2\|\mathbf{k}\|^2\|W_2\|^2_\infty\|q_{2,h}\|^2_{0,\Gamma_K}\\
&\quad\le C_1\frac{2\kappa_1^2\|\mathbf{k}\|^2\|W_1\|^2_\infty h^2|\Gamma_K|}{|K_1|}\|\nabla q_{1,h}\|^2_{0,K_1}+\\
&C_2\frac{2\kappa_2^2\|\mathbf{k}\|^2\|W_2\|^2_\infty h^2|\Gamma_K|}{|K_2|}\|\nabla q_{2,h}\|^2_{0,K_2}\\
&\quad=2hC_1\kappa_1\|\mathbf{k}\|^2\|W_1\|_\infty\lambda_K\|\nabla q_{1,h}\|^2_{0,K_1}\\
&\qquad+2hC_2\kappa_2\|\mathbf{k}\|^2\|W_2\|_\infty\lambda_K\|\nabla q_{2,h}\|^2_{0,K_2}\\
&\quad\le C_3h\|\mathbf{k}\|^2\lambda_K\|W\|_\infty\left(\kappa_1\|\nabla q_{1,h}\|^2_{0,K_1}+\kappa_2\|\nabla q_{2,h}\|^2_{0,K_2}\right)\\
&\quad\le C_3h\|\mathbf{k}\|^2\lambda_K\|W\|_\infty\|\nabla q_h\|^2_{0,K_1\cup K_2};
\end{aligned}\tag{3.28}$$

where we have used the fact $\kappa_i\le 1$ in the last inequality. This completes the proof of inequality (3.26) and the inequality (3.27) can be established by a similar argument. □

Now, we are ready to show that the bilinear form $a_h(\cdot,\cdot)$ is coercive and continuous with respect to the above mesh-dependent norm in the following sense:

Theorem 2 *Suppose that the stability parameter $\hat{\lambda}$ is large enough. Then there exist two constants C_5 and C_6 such that*

$$C_5|||q_h|||_h^2\le a_h(q_h,q_h),\quad\forall q_h\in V_{h,per};\tag{3.29}$$

$$a_h(q_h,\chi_h)\le C_6|||q_h|||_h|||\chi_h|||_h,\quad\forall q_h,\chi_h\in V_{h,per}.\tag{3.30}$$

Proof It is noted that (3.30) is a direct consequence of Lemma 3. So we only need to justify the inequality (3.29). Letting $\phi_h=q_h$ in (3.17) and applying the Cauchy–Scharwz inequality and the Young's inequality with ϵ, we have

$$\begin{aligned}
&a_h(q_h,q_h)\\
&=\sum_{i=1}^{2}\int_{\Omega_i}W(\nabla+\mathbf{i}\mathbf{k})q_h\cdot\overline{(\nabla+\mathbf{i}\mathbf{k})q_h}d\mathbf{x}\\
&\quad-2\mathrm{Re}\int_\Gamma\{\!\{W(\nabla+\mathbf{i}\mathbf{k})q_h\cdot n\}\!\}[\![\overline{q_h}]\!]ds+\frac{1}{h}\|\lambda^{1/2}[\![q_h]\!]\|^2_{0,\Gamma}\\
&\ge\|W^{1/2}(\nabla+\mathbf{i}\mathbf{k})q_h)\|^2_{0,\Omega_1\cup\Omega_2}-2\|\{\!\{W(\nabla+\mathbf{i}\mathbf{k})q_h\cdot\mathbf{n}\}\!\}\|_{0,\Gamma}\|[\![q_h]\!]\|_{0,\Gamma}+\frac{1}{h}\|\lambda^{1/2}[\![q_h]\!]\|^2_{0,\Gamma}\\
&\ge C_u\|(\nabla+\mathbf{i}\mathbf{k})q_h)\|^2_{0,\Omega_1\cup\Omega_2}-\sum_{K\in\mathcal{T}_{\Gamma,h}}\frac{h}{\epsilon\lambda_K}\|\{\!\{W(\nabla+\mathbf{i}\mathbf{k})q_h\cdot\mathbf{n}\}\!\}\|^2_{0,\Gamma_K}\\
&\quad+\sum_{K\in\mathcal{T}_{\Gamma,h}}\frac{(\hat{\lambda}-\epsilon)\lambda_K}{h}\|[\![q_h]\!]\|^2_{0,\Gamma_K}\\
&\ge C_u\|(\nabla+\mathbf{i}\mathbf{k})q_h)\|^2_{0,\Omega_1\cup\Omega_2}-\sum_{K\in\mathcal{T}_{\Gamma,h}}\frac{2h}{\epsilon\lambda_K}\|\{\!\{(W\nabla q_h)\cdot\mathbf{n}\}\!\}\|^2_{0,\Gamma_K}
\end{aligned}$$

$$- \sum_{K\in\mathcal{T}_{\Gamma,h}} \frac{2h}{\epsilon\lambda_K}\|\{\{(W\mathbf{k}q_h)\cdot\mathbf{n}\}\}\|^2_{0,\Gamma_K} + \sum_{K\in\mathcal{T}_{\Gamma,h}} \frac{(\hat{\lambda}-\epsilon)\lambda_K}{h}\|[\![q_h]\!]\|^2_{0,\Gamma_K}.$$

Then, using Lemma 3, we can deduce that

$$\begin{aligned}
&a_h(q_h,q_h)\\
&\geq C_u\|(\nabla+\mathrm{i}\mathbf{k})q_h)\|^2_{0,\Omega_1\cup\Omega_2} + \sum_{K\in\mathcal{T}_{\Gamma,h}} \frac{(\hat{\lambda}-\epsilon)\lambda_K}{h}\|[\![q_h]\!]\|^2_{0,\Gamma_K}\\
&\quad - \sum_{K\in\mathcal{T}_{\Gamma,h}} \frac{2(C_3\|\mathbf{k}\|^2h^2+C_4)}{\epsilon}\|W\|_\infty\|\nabla q_h\|^2_{0,K_1\cup K_2}\\
&\geq C_u\|(\nabla+\mathrm{i}\mathbf{k})q_h)\|^2_{0,\Omega_1\cup\Omega_2} + \sum_{K\in\mathcal{T}_{\Gamma,h}} \frac{(\hat{\lambda}-\epsilon)\lambda_K}{h}\|[\![q_h]\!]\|^2_{0,\Gamma}\\
&\quad - \frac{2(16C_3+C_4)}{\epsilon}\|W\|_\infty\|q_h\|^2_{1,\Omega_1\cup\Omega_2}\\
&\geq \frac{1}{2}C_u\|(\nabla+\mathrm{i}\mathbf{k})q_h)\|^2_{0,\Omega_1\cup\Omega_2} + \sum_{K\in\mathcal{T}_{\Gamma,h}} \frac{(\hat{\lambda}-\epsilon)\lambda_K}{h}\|[\![q_h]\!]\|^2_{0,\Gamma}\\
&\quad + \left(\frac{1}{2}C_u - \frac{2C_I(16C_3+C_4)}{\epsilon}\|W\|_\infty\right)\|(\nabla+\mathrm{i}\mathbf{k})q_h)\|^2_{0,\Omega_1\cup\Omega_2}.
\end{aligned}$$

Here, C_I is the constant such that $\|q_h\|^2_{1,\Omega_1\cup\Omega_2} \leq C_I\|(\nabla+\mathrm{i}\mathbf{k})q_h)\|^2_{0,\Omega_1\cup\Omega_2}$ for fixed nonzero $\mathbf{k}$ and we have used the fact $\|\mathbf{k}\| \leq 4$ in the first inequality. We conclude our proof of (3.29) by taking $\epsilon = \frac{4C_I(16C_3+C_4)}{C_u}\|W\|_\infty$ and choosing the stability parameter $\hat{\lambda} > \epsilon$. □

Theorem 2 implies that the finite element eigenvalue value problem (3.16) is well-posed. According to the spectral theory, the discrete eigenvalue of (3.16) can be enumerated as

$$0 < E^1_h(\mathbf{k}) \leq E^2_h(\mathbf{k}) \leq \cdots E^{n_h}_h(\mathbf{k}) \tag{3.31}$$

and the corresponding L^2-orthonormal eigenfunctions are $\phi^1_h, \phi^2_h, \ldots, \phi^{n_h}_h$. Here, n_h is the dimension of the unfitted Nitsche's finite element space $V_{h,per}$, i.e. $n_h = \dim V_{h,per}$.

The key in the interpolation error estimations of the unfitted Nitsche's methods is to extend a function in the subdomain Ω_i to the whole domain Ω. For any $q \in H^2(\Omega_i)$, the extension operator of ϕ from $H^2(\Omega_i)$ to $H^2(\Omega)$ is denoted by X_i which satisfies

$$(X_iq)|_{\Omega_i} = q \tag{3.32}$$

and

$$\|X_iq\|_{s,\Omega} \leq C\|q\|_{s,\Omega_i}, \quad \text{for } s = 0, 1, 2. \tag{3.33}$$

Let $I_{i,h}$ be the standard nodal interpolation operator from $C(\overline{\Omega})$ to $V_{i,h}$. Define the interpolation operator for the finite element space V_h as

$$I^*_hq = (I^*_{1,h}q_1, I^*_{2,h}q_2), \tag{3.34}$$

where

$$I^*_{i,h}q = I_{i,h}X_iq_i,\ i = 1, 2. \tag{3.35}$$

For the linear interpolation operator, [18] established the following optimal error estimates:

$$\|q - I_h^* q\|_{0,\Omega} + h|||q - I_h^* q|||_h \leq Ch^2 \|q\|_{2,\Omega_1 \cup \Omega_2}. \tag{3.36}$$

3.2 Unfitted Nitsche's Method for Computing Edge Modes

In this subsection, we generalize the unfitted Nitsche's method introduced in previous subsection to compute edge modes. Similarly, to model the wave propagation in the heterogeneous media, we will adopt the jump conditions. Let Γ_Σ be the union of interfaces in all cells in the fundamental domain of the cylinder. Based on this setup, edge states are the eigenpair of the following interface eigenvalue problem

$$\mathcal{L}^W \Psi(\mathbf{x}; k_\parallel) = E(k_\parallel)\Psi(\mathbf{x}; k_\parallel), , \tag{3.37}$$

$$\Psi(\mathbf{x} + \mathbf{v}_1; k_\parallel) = e^{\mathrm{i}k_\parallel} \Psi(\mathbf{x}; k_\parallel), \tag{3.38}$$

$$\Psi(\mathbf{x}; k_\parallel) \to 0 \ \text{ as } \ |\mathbf{x} \cdot \mathbf{k}_2| \to \infty, \tag{3.39}$$

$$[\![\Psi]\!] = [\![W \nabla \Psi \cdot n]\!] = 0, \quad \text{on } \Gamma_\Sigma. \tag{3.40}$$

on the infinite domain Ω_Σ.

For the interface eigenvalue problem (3.37)–(3.40), the numerical challenges not only stem from the heterogeneity of the media and the quasi-periodicity of the boundary condition but also stem from the infinity nature of the cylindrical domain. For the second difficulty, thanks to the localization property of the eigenfunction in the $\mathbf{v}_2$ direction, we can truncate the infinite cylinder into a finite computational domain and replace the localization condition (3.39) by a homogeneous Dirichlet boundary condition. We remark that this truncation will introduce some error between the eigenvalue problems defined in the finite domain and infinite domain. Pseudo edge-states located at the truncated boundaries will appear. How to analyze the truncation error and avoid the pseudo states are interesting problems which have been partially discussed recently. We refer interested readers to [30,40] for more details. Our work mainly focuses on the numerical scheme and associated error analysis of the truncated problem. In particular, we define the truncated domain $\Omega_{\Sigma,L}$ as

$$\Omega_{\Sigma,L} \equiv \{\tau_1 \mathbf{v}_1 + \tau_2 \mathbf{v}_2 : 0 \leq \tau_1 \leq 1, -L \leq \tau_2 \leq L\}. \tag{3.41}$$

To handle the quasi-periodic boundary condition on $\mathbf{v}_1$ direction, we apply the Floquet-Bloch transformation $\Psi(\mathbf{x}; k_\parallel) = e^{\mathrm{i}\frac{k_\parallel}{2\pi}\mathbf{k}_1 \cdot \mathbf{x}} \psi(\mathbf{x}; k_\parallel)$. Then, we reformulate the problem of finding edge states as computing the eigenpairs of the interface eigenvalue problem

$$\mathcal{L}^W(k_\parallel)\psi(\mathbf{x}; k_\parallel) = E(k_\parallel)\psi(\mathbf{x}; k_\parallel), \tag{3.42}$$

$$\psi(\mathbf{x} + \mathbf{v}_1; k_\parallel) = \psi(\mathbf{x}; k_\parallel), \tag{3.43}$$

$$\psi(\tau_1 \mathbf{v}_1 \pm L\mathbf{v}_2; k_\parallel) = 0, \forall\, 0 \leq \tau_1 \leq 1, \tag{3.44}$$

$$[\![\psi]\!] = [\![W(\nabla + \mathrm{i}\mathbf{k})\psi \cdot n]\!] = 0, \quad \text{on } \Gamma_\Sigma. \tag{3.45}$$

where

$$\mathcal{L}^W(k_\parallel) = -(\nabla + \mathrm{i}\frac{k_\parallel}{2\pi}\mathbf{k}_1) \cdot W(\nabla + \mathrm{i}\frac{k_\parallel}{2\pi}\mathbf{k}_1). \tag{3.46}$$

Fig. 3 Plot of the interface $\Gamma_{\Sigma,L}$ with $\mathbf{v}_2$ being the x-axis and $\mathbf{v}_1$ being the y-axis

3.2.1 Unfitted Nitsche's Method on a Cylinder

To present unfitted Nitsche's method on the truncated domain $\Omega_{\Sigma,L}$, we introduce the corresponding Sobolev spaces. Let $W^{k,p}(\Omega_{\Sigma,L})$ denote the Sobolev spaces of functions defined on $\Omega_{\Sigma,L}$ with norm $\|\cdot\|_{k,p}$ and seminorm $|\cdot|_{k,p}$. To incorporate the boundary conditions, we define

$$W^{k,p}_{per}(\Omega_{\Sigma,L}) \equiv \{\psi : \psi \in W^{k,p}(\Omega_{\Sigma,L}) \text{ and } \psi(\mathbf{x}+\mathbf{v}_1) = \psi(\mathbf{x})\}, \tag{3.47}$$

and

$$W^{k,p}_{per,0}(\Omega_{\Sigma,L}) \equiv \{\psi : \psi \in W^{k,p}_{per} \text{ and } \psi(\tau_1\mathbf{v}_1 \pm L\mathbf{v}_2) = 0 \text{ for } 0 \le \tau_1 \le 1\}. \tag{3.48}$$

When $p = 2$, it is simply denoted as $H^k_{per}(\Omega_{\Sigma,L})$ or $H^k_{per,0}(\Omega_{\Sigma,L})$.

Note the fact that $\epsilon(\mathbf{x})$ is Λ-periodic. Then, the computational domain $\Omega_{\Sigma,L}$ can be split into two disjoint subdomains $\Omega^1_{\Sigma,L}$ and $\Omega^2_{\Sigma,L}$, where

$$\Omega^i_{\Sigma,L} = \Omega_{\Sigma,L} \cap (\Omega_i + \Lambda), \tag{3.49}$$

for $i = 1, 2$. The restriction of the interface Γ_Σ in $\Omega_{\Sigma,L}$ is denoted by $\Gamma_{\Sigma,L}$, i.e. $\Gamma_{\Sigma,L} = \Omega^1_{\Sigma,L} \cap \Omega^2_{\Sigma,L}$. In Fig. 3, we give a plot of the interface $\Gamma_{\Sigma,L}$ with $L = 10$.

Let $\hat{\mathcal{T}}_h$ denote the uniform triangular partition of the computational domain $\Omega_{\Sigma,L}$. The mesh $\hat{\mathcal{T}}_h$ is generated by firstly dividing $\Omega_{\Sigma,L}$ into $2LN^2$ sub-rhombuses with mesh size $h = \frac{\|\mathbf{v}_1\|}{N}$ and splitting each sub-rhombus into two triangles. Similarly, the elements in mesh $\hat{\mathcal{T}}_h$ can be classified as regular elements or interface elements. Let $\hat{\mathcal{T}}_{i,h}$ be the set all elements in $\hat{\mathcal{T}}_h$ covering the subdomain $\Omega^i_{\Sigma,L}$ for $i = 1, 2$ and $\hat{\mathcal{T}}_{\Gamma,h}$ be the set of interface elements. The union of all elements in $\hat{\mathcal{T}}_{i,h}$ is denoted by $\Omega^i_{\Sigma,L,h}$, which is defined as

$$\Omega^i_{\Sigma,L,h} = \bigcup_{K \in \hat{\mathcal{T}}_{i,h}} K, \quad i = 1, 2. \tag{3.50}$$

As demonstrated in the previous section, $\Omega^1_{\Sigma,L,h}$ and $\Omega^2_{\Sigma,L,h}$ form an overlapping decomposition of the computational domain $\Omega_{\Sigma,L}$.

To introduce the finite element space for the unfitted Nitsche's method, we begin with defining the finite element space on each fictitious subdomain $\Omega^i_{\Sigma,L}$. Let $\hat{V}_{i,h}$ be the standard continuous finite element space on $\Omega^i_{\Sigma,h}$ which is defined as

$$\hat{V}_{i,h} = \left\{ v \in C^0(\Omega^i_{\Sigma,h}) : v|_K \in \mathbb{P}_1(K) \text{ for any } K \in \hat{\mathcal{T}}_{i,h} \right\}, \ i = 1, 2. \tag{3.51}$$

Then, the unfitted Nitsche's finite element space $\hat{V}_h$ is the direct sum of $\hat{V}_{1,h}$ and $\hat{V}_{2,h}$, i.e. $\hat{V}_h = \hat{V}_{1,h} \oplus \hat{V}_{2,h}$. To impose the periodic boundary condition in $\mathbf{v}_1$ direction and homogeneous Dirichlet boundary condition in $\mathbf{v}_2$ direction, we introduce the subspace $\hat{V}_{h,0} = \hat{V}_h \cap H^k_{per,0}(\Omega_{\Sigma,L})$.

Similar to the previous section, we define unfitted Nitsche's bilinear form $\hat{a}_h(\cdot,\cdot)$ as

$$\begin{aligned}\hat{a}_h(u_h,v_h) = &\sum_{i=1}^{2}\int_{\Omega^i_{\Sigma,L}} W\left(\nabla + \mathrm{i}\frac{k_\parallel}{2\pi}\mathbf{k}_1\right)u_h \cdot \overline{\left(\nabla + \mathrm{i}\frac{k_\parallel}{2\pi}\mathbf{k}_1\right)v_h}d\mathbf{x}\\ &- \int_{\Gamma_{\Sigma,L}}\left\{\left\{W\left(\nabla + \mathrm{i}\frac{k_\parallel}{2\pi}\mathbf{k}_1\right)u_h\cdot n\right\}\right\}[\![\overline{v_h}]\!]ds\\ &- \int_{\Gamma_{\Sigma,L}}\left\{\left\{\overline{W\left(\nabla + \mathrm{i}\frac{k_\parallel}{2\pi}\mathbf{k}_1\right)v_h\cdot n}\right\}\right\}[\![u_h]\!]ds\\ &+ \frac{1}{h}\int_{\Gamma_{\Sigma,L}}\lambda[\![u_h]\!][\![\overline{v_h}]\!]ds,\end{aligned}$$

for any functions u_h, v_h in $\hat{V}_h$. Then, the unfitted Nitsche's method for the interface eigenvalue problem is to find the eigenpair $(\psi_h, E(k_\parallel))$ such that

$$\hat{a}_h(\psi_h,\eta_h) = E_h(k_\parallel)\hat{b}(\psi_h,\eta_h), \quad \forall\eta_h \in \hat{V}_{h,0}; \tag{3.52}$$

where

$$\hat{b}(\psi_h,\eta_h) = \int_{\Omega_\Gamma}\psi_h\cdot\overline{\eta_h}d\mathbf{x}. \tag{3.53}$$

3.2.2 Well-Posedness of Unfitted Nitsche's Method on a Cylinder

Using the same argument as in previous subsection, we can prove the unfitted Nitsche's weak form (3.52) is consistent in the following sense:

Lemma 4 *Let $(\psi, E(k_\parallel))$ be the eigenpair of the interface eigenvalue problem (3.3)–(3.4). Then $(\psi, E(k_\parallel)) \in H^1_{per,0}(\Omega_{\Sigma,L})\times\mathbb{R}$ also satisfies*

$$\hat{a}_h(\psi,\eta) = E(k_\parallel)\hat{b}(\psi,\eta), \quad \forall\eta\in H^1_{per,0}(\Omega_{\Sigma,L}). \tag{3.54}$$

Let us consider the following truncated interface source problem

$$\mathcal{L}^W(k_\parallel)u(\mathbf{x}) = f(\mathbf{x}), \tag{3.55}$$

$$u(\mathbf{x}+\mathbf{v}_1) = u(\mathbf{x}), \tag{3.56}$$

$$u(\tau_1\mathbf{v}_1 \pm L\mathbf{v}_2) = 0, \forall\, 0\le\tau_1\le 1, \tag{3.57}$$

$$[\![u]\!] = [\![W(\nabla+\mathrm{i}\mathbf{k})u\cdot n]\!] = 0, \quad \text{on } \Gamma_\Sigma. \tag{3.58}$$

As a direct consequence of the above Lemma, we have the following Galerkin orthogonality for the source problem:

Corollary 2 *Let u be the solution of the interface problem (3.55)–(3.58) and u_h be the corresponding finite element approximation by the unfitted Nitsche's method. Then we have*

$$\hat{a}_h(u-u_h,v_h) = 0, \quad \forall v_h\in\hat{V}_{h,0}. \tag{3.59}$$

We also introduce the following energy norm

$$|||\psi|||_h^2 = \|(\nabla+\mathrm{i}\frac{k_\parallel}{2\pi}\mathbf{k}_1)\psi\|^2_{0,\Omega^1_{\Sigma,L}\cap\Omega^2_{\Sigma,L}} + \sum_{K\in\hat{\mathcal{T}}_{\Gamma,h}} h^{-1}\|[\![\psi]\!]\|^2_{0,\Gamma_K}. \tag{3.60}$$

In term of the energy norm, we shall show that the unfitted Nitsche's bilinear form is coercive and continuous in the following sense

Theorem 3 *Suppose the stability parameter $\hat{\lambda}$ is large enough. Then there are two constants C_7 and C_8 such that*

$$C_7|||q_h|||_h^2 \le \hat{a}_h(q_h, q_h), \quad \forall q_h \in \hat{V}_h; \tag{3.61}$$

$$\hat{a}_h(q_h, \chi_h) \le C_8|||q_h|||_h|||\chi_h|||_h, \quad \forall q_h, \chi_h \in \hat{V}_{h,0}. \tag{3.62}$$

Theorem 3 also means the discrete eigenvalue value problem (3.16) is a well-posed problem. According to the spectral theory, the discrete eigenvalue of (3.16) can be enumerated as

$$0 < E_h^1(k_\parallel) \le E_h^2(k_\parallel) \le \cdots E_h^{\hat{n}_h}(k_\parallel) \tag{3.63}$$

and the corresponding L^2-orthonormal eigenfunctions are $\psi_h^1, \psi_h^2, \ldots, \psi_h^{\hat{n}_h}$. Here, $\hat{n}_h$ is the dimension of the unfitted Nitsche's finite element space $\hat{V}_{h,0}$.

Likewise, we use $\hat{X}_i$ to denote the extension operator for functions defined $\Omega_{\Sigma,L}^i$ to $\Omega_{\Sigma,L}$ which satisfies

$$(\hat{X}_i\eta)|_{\Omega_i} = \eta \tag{3.64}$$

and

$$\|\hat{X}_i\eta\|_{s,\Omega} \le C\|q\|_{s,\Omega_i}, \quad \text{for } s = 0, 1, 2. \tag{3.65}$$

Let $\hat{I}_{i,h}$ be the standard nodal interpolation operator from $C(\overline{\Omega_{\Sigma,L}})$ to $\hat{V}_{i,h}$. Define the interpolation operator for the finite element space $\hat{V}_h$ as

$$\hat{I}_h^* q = (\hat{I}_{1,h}^* q_1, \hat{I}_{2,h}^* q_2), \tag{3.66}$$

where

$$\hat{I}_{i,h}^* q_i = \hat{I}_{i,h}\hat{X}_i q_i, \ i = 1, 2. \tag{3.67}$$

We can also show the following interpolation error estimates:

$$\|\eta - \hat{I}_h^*\eta\|_{0,\Omega_{\Sigma,L}} + h|||\eta - \hat{I}_h^*\eta|||_h \le Ch^2\|\eta\|_{2,\Omega_{\Sigma,L}^1 \cup \Omega_{\Sigma,L}^2}. \tag{3.68}$$

4 Error Analysis

In this section, we present unified error estimation for the proposed unfitted Nitsche's methods. Our main analysis tool is the Babuška-Osborn spectral approximation theory [6].

When we consider the eigenvalue problem (3.3)–(3.4), let $A_h(\cdot,\cdot)$ denote the Nitsche's bilinear function $a_h(\cdot,\cdot)$ which is defined on $V_a := H_{per}^1(\Omega)$ and $B_h(\cdot,\cdot)$ corresponding the L^2 inner production $b_h(\cdot,\cdot)$ on $V_b := L_{per}^2(\Omega)$. Similarly, when we consider the eigenvalue problem (3.42)–(3.45), let $A_h(\cdot,\cdot)$ denote denote the Nitsche's bilinear function $\hat{a}_h(\cdot,\cdot)$ which is defined on $V_a := H_{per,0}^1(\Omega_{\Sigma,L})$ and $B_h(\cdot,\cdot)$ corresponding the L^2 inner production $\hat{b}_h(\cdot,\cdot)$ on $V_b := L_{per}^2(\Omega_{\Sigma,L})$. The corresponding L^2 norm is denoted by $\|\cdot\|_b$. The Nitsche's finite element function is denote by S_h which is either $V_{h,per}$ or $\hat{V}_{h,0}$.

For any $f \in V_b$, let $T : V_b \to V_a$ be the solution operator for the source problem such that

$$A_h(Tf, g) = (f, g), \quad \forall g \in V_a. \tag{4.1}$$

We rewrite the interface eigenvalue problem (3.3)–(3.4) [or (3.42)–(3.45)] as

$$T\phi = \mu\phi \tag{4.2}$$

where $\mu = E(\mathbf{k})^{-1}$ (or $\mu = E(k_\parallel)^{-1}$). For the source problem (4.1), we can show the following regularity [5,22]

$$\|Tf\|_{2,\star} \le C\|f\|_b, \tag{4.3}$$

where the notation $\|\cdot\|_{2,\star}$ denotes the piecewise H^2 norm $\|\cdot\|_{2,\Omega_1\cup\Omega_2}$ or $\|\cdot\|_{2,\Omega^1_{\Sigma,L}\cup\Omega^2_{\Sigma,L}}$.

Similarly, we introduce the solution operator T_h for the discrete source problems which is defined as

$$a_h(T_h f, g_h) = (f, g_h), \quad \forall g_h \in S_h. \tag{4.4}$$

The unfitted Nitsche's method (3.16) has the following equivalent representation

$$T_h\phi_h = \mu_h\phi_h, \tag{4.5}$$

where $\mu_h = E_h(\mathbf{k})^{-1}$ (or $\mu_h = E_h(k_\parallel)^{-1}$). Evidently, both T and T_h are self-adjoint, elliptic, and compact linear operators.

From the interpolation error estimate, we can show the following error estimates for unfitted Nitsche's method approximating the source problem:

Theorem 4 *Let T and T_h be the solution operators defined in (4.1) and (4.4), respectively. Then we have the following error estimates, for any $f \in L^2(\Omega)$ (or $L^2(\Omega_{\Sigma,L})$),*

$$|||Tf - T_h f|||_h \le Ch\|f\|_b, \tag{4.6}$$

$$\|Tf - T_h f\|_b \le Ch^2\|f\|_b. \tag{4.7}$$

Proof The inequality (4.6) follows directly from Theorem 2 (or Theorem 3), the interpolation error estimate (3.36) [or (3.68)], and the regularity (4.3). The inequality (4.7) can be proved via the Aubin-Nitsche's tricks, see for example, [18]. □

From the above theorem, we can deduce the following corollary:

Corollary 3 *Let T and T_h be the solution operator defined in (4.1) and (4.4), respectively. We have*

$$||T - T_h||_{\mathcal{L}(V_b)} \le Ch^2. \tag{4.8}$$

and thus

$$\lim_{h\to 0} ||T - T_h||_{\mathcal{L}(V_b)} = 0. \tag{4.9}$$

Let $\rho(T)$ (or $\rho(T_h)$) denote the resolvent set of operator T (or T_h), and $\sigma(T)$ (or $\sigma(T_h)$ denote the spectrum set of operator T (or T_h). Using the above approximation property, we have the following property of no pollution of the spectrum which is a direct application of Theorem 9.1 in [7]:

Theorem 5 *For any compact set $K \subset \rho(T)$, there is $h_0 > 0$ such that $K \subset \rho(T_h)$ holds for all $h < h_0$. If E is a nonzero eigenvalue of T with algebraic multiplicity m, there are m eigenvalues $E_h^1, E_h^1, \cdots, E_h^m$ of T_h such that all eigenvalues E_h^j, $j = 1, \ldots, m$ converge to E as h tends to 0.*

For any closed smooth curve $\mathcal{C} \subset \rho(T)$ enclosing $E \in \sigma(T)$ and no other element of $\sigma(T)$, the Reisz spectral projection associated with E is defined as [6]

$$P = \frac{1}{2\pi \mathrm{i}} \int_{\mathcal{C}} (z - T)^{-1} dz. \tag{4.10}$$

Let $R(P)$ be the range of the Reisz spectral projection P. When h is sufficiently small, $\mathcal{C} \subset \rho(T_h)$ encloses exactly m discrete eigenvalues of T_h. We define analogously the discrete spectral projection

$$P_h = \frac{1}{2\pi \mathrm{i}} \int_{\mathcal{C}} (z - T_h)^{-1} dz. \tag{4.11}$$

Thanks to the above preparations, we are ready to show our main eigenpair approximation results.

Theorem 6 *Let μ_h be an eigenvalue of T_h such that $\lim_{h\to 0} \mu_h = \mu$. Let g_h be a unit eigenvector of T_h corresponding to the eigenvalue μ_h. Then there exists a unit eigenvector $g \in R(P)$ such that the following estimates hold*

$$\|g - g_h\|_{0,\Omega} \le Ch^2 \|g\|_{2,\star}, \tag{4.12}$$

$$|\mu - \mu_h| \le Ch^2 \|g\|_{2,\star}, \tag{4.13}$$

$$|E - E_h| \le Ch^2 \|g\|_{2,\star}. \tag{4.14}$$

Proof In order to justify the estimate (4.12), we apply the Theorem 7.4 in [6] and the operator approximation result (4.7), and deduce that

$$\|g - g_h\|_{0,\Omega} \le \|(T - T_h)|_{R(P)}\|_b = \sup_{\substack{q \in R(P) \\ \|\|q\|\|_h = 1}} \|Tq - T_h q\|_{0,\Omega} \le Ch^2 \|\phi\|_{2,\star},$$

which completes the proof of (4.12).

Then, we turn to the estimate (4.13). Let $v_1, \ldots, v_m$ be any basis for $R(P)$. Then, Theorem 7.3 in [6] implies that there exists a constant C such that

$$|\mu - \mu_h| \le C \sum_{j,k=1}^{m} |((T - T_h)v_j, v_k)| + C\|(T - T_h)|_{R(P)}\|_{0,\Omega}^2. \tag{4.15}$$

To establish upper bound for $|\mu - \mu_h|$, it is sufficient to bound the first term in (4.15). Using (4.1), (4.4) and the Galerkin orthogonality (3.22) [or (3.59)], we obtain the (4.13) by

the following calculations

$$\begin{aligned}((T-T_h)v_j, v_k) =&(v_j, (T-T_h)v_k)\\ =&a_h(Tv_j, Tv_k - T_h v_k)\\ =&a_h(Tv_j - T_h v_j, Tv_k - T_h v_k) + a_h(T_h v_j, Tv_k - T_h v_k)\\ =&a_h(Tv_j - T_h v_j, Tv_k - T_h v_k) + \overline{a_h(Tv_k - T_h v_k, T_h v_j)}\\ =&a_h(Tv_j - T_h v_j, Tv_k - T_h v_k)\\ \le& C|||Tv_j - T_h v_j|||_h |||Tv_k - T_h v_k|||_h\\ \le& Ch^2 \|v_j\|_{2,\star}\|v_k\|_{2,\star}\\ \le& Ch^2\|g\|^2_{2,\star}.\end{aligned} \tag{4.16}$$

The last estimate (4.14) is actually a direct consequence of (4.13) by recalling that $\mu = E^{-1}$ (or $\mu_h = E_h^{-1}$). □

5 Numerical Examples

In this section, we present a series of benchmark numerical examples to verify and validate our theoretical results and demonstrate that the proposed unfitted Nitsche's methods are effective and efficient numerical methods to compute the dispersion relation and wave modes for topological materials with very high contrast material weights.

5.1 Numerical Examples for Computing Dispersion Relations

In this subsection, we numerically investigate the performance of the unfitted Nitsche's method for computing the dispersion relations of the bulk on a torus, i.e. the material weight is Λ-periodic. We choose the material weight W in (2.8) with

$$\epsilon(\mathbf{x}) = \begin{cases} 1+J, & \text{if } \mathbf{x} \in \Omega_1,\\ 1, & \text{if } \mathbf{x} \in \Omega_2.\end{cases}$$

The jump ratio of the material coefficient is $(1+J)^2$. For large J, we have high contrast material weight. The radius of $B_r(\mathbf{A})$ and $B_r(\mathbf{B})$ is chosen to be 0.2.

5.1.1 Verification of Accuracy

In this part, we run a series of tests to show the optimal convergence of the numerical eigenvalue obtained by the unfitted Nitsche's method. To measure the errors, we introduce the following relative error of eigenvalues

$$e_i = \frac{|E_{i,h_j}(\mathbf{k}) - E_{i,h_{j+1}}(\mathbf{k})|}{E_{i,h_{j+1}}(\mathbf{k})}.$$

Different values of J and γ are chosen to test our numerical methods. The numerical errors of the first four eigenvalues are plotted in Figs. 4 and 5, where the numerical eigenvalues converge at the optimal rate $\mathcal{O}(h^2)$. This confirms that the error estimate for the unfitted Nitsche's method is uniform with respect to the jump ratio $(J+1)^2$.

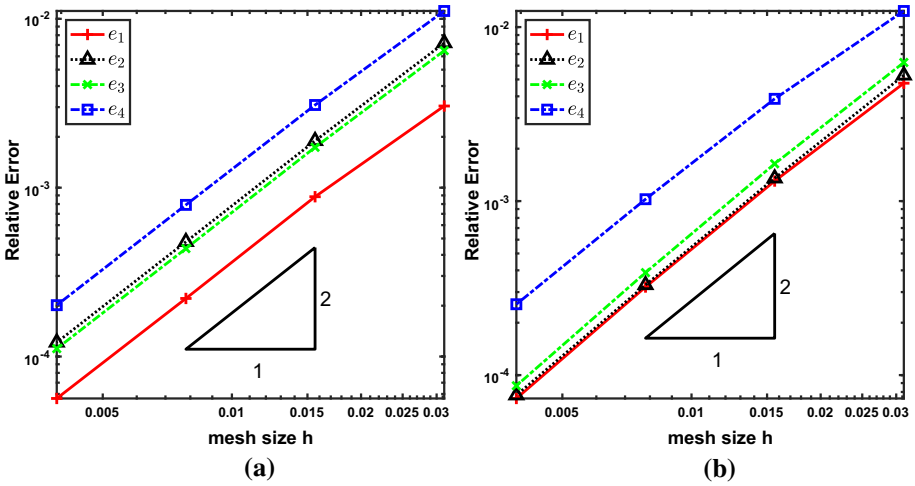

Fig. 4 Numerical errors for eigenvalue approximation: **a** $J = 2$ and $\gamma = 0$; **b** $J = 2$ and $\gamma = 0.1$

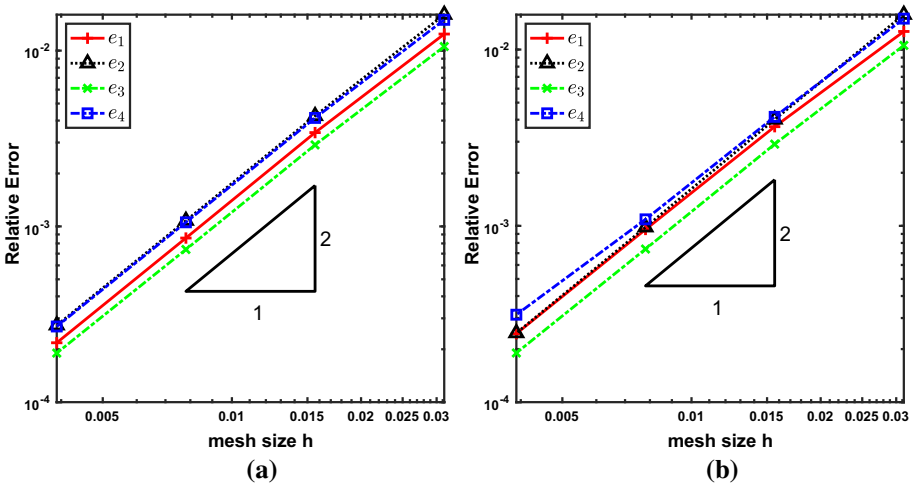

Fig. 5 Numerical errors for eigenvalue approximation: **a** $J = 100$ and $\gamma = 0$; **b** $J = 100$ and $\gamma = 0.1$

5.1.2 Numerical Investigation of the Dispersion Relations

In this part, we compute the dispersion relations of the bulk and make comparisons with the Fourier spectral methods [24,38], which expands both the material weight $W(\mathbf{x})$ and eigenfunctions in terms of Fourier series. For the unfitted Nitsche's method, we use the meshes with mesh size $h = \frac{1}{64}$. For the Fourier spectral method, we use at least 16 Fourier modes in each direction. The computed eigenvalues using Fourier spectral methods are denoted by $\tilde{E}_i$ $(i = 1, 2, 3)$ in Fig. 7.

As mentioned in Sect. 2.2, there exists a Dirac point near $\mathbf{K} = \frac{1}{3}(\mathbf{k}_1 - \mathbf{k}_2)$ and $\mathbf{K}' = -\mathbf{K}$ when $\lambda = 0$. To observe this mechanism, we plot the eigenvalue $E_m(\mathbf{k})$ with $\mathbf{k} = \mathbf{K} + \tau\mathbf{k}_1$ in term of τ (the x-axis in Figs. 6 and 7), which is termed as eigencurve, for $m = 1, 2, 3$.

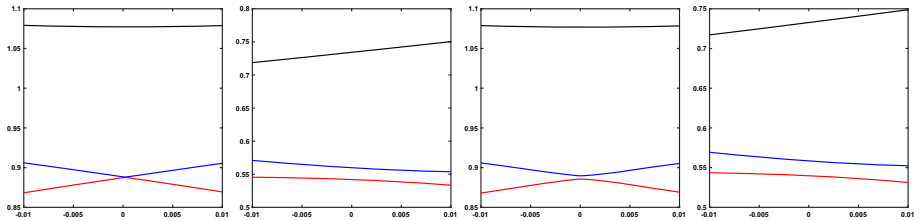

Fig. 6 Dispersion relations when $J = 30$: **a** Unfitted Nitsche's Method with $\gamma = 0$; **b** Spectral Method with $\gamma = 0$; **c** Unfitted Nitsche's Method with $\gamma = 0.1$; **d** Spectral Method with $\gamma = 0.1$

We directly consider the case with a relatively large jump ratio with $J = 30$. The numerical results are displayed in Fig. 6. For the unfitted Nitsche's method, we observe the existence of the Dirac point for $\gamma = 0$ and the disappearance of the Dirac point when $\gamma = 0.1$. This agrees well with the theoretical results [24]. Unfortunately, the Fourier spectral method fails to give the correct results. In particular, we can see that a gap between the first eigencurve and the second eigencurve opens up when $\gamma = 0$ and that the eigencurves are not symmetric which clearly violates the mathematical theory of the spectrum [24]. The performance is not improved even when we increase the number of Fourier modes in each direction.

For small jump ratio case, the Fourier spectral method seems to give a reliable result. We will see that our method can do a much better job. To make a quantitative comparison of those two methods for the small jump ratio case, we graph the results of those two methods in the same plot when $J = 2$ in Fig. 7. In the Figure, the numerical results generated by the unfitted Nitsche's method are plotted by solid curves and the numerical results generated by the Fourier spectral method are represented by dashed curves. We can see that the numerical eigenvalues given by the unfitted Nitsche's method are lower than the counterpart given by the Fourier spectral methods. This observation implies that the unfitted Nitsche's method is much more accurate than the Fourier spectral method since both methods are Galerkin methods which give upper bounds of the exact eigenvalues.

In summary, though the Fourier spectral method is widely used in photonic community, it is not a good numerical method to handle the discontinuous material weight, especially when the jump ration is large. In contrast, the unfitted Nitsche's method can give very reliable results in spite of arbitrary large jump ratio.

5.2 Numerical Examples for Computing Edge Modes

In this subsection, we present numerical examples to show the unfitted Nitsche's method proposed in Sect. 4 is an efficient numerical method for computing topologically protected edge modes with high contrast material weight on a cylinder and supports the theoretical result for eigenvalue approximation. We consider the material weight given in the form

$$W(\mathbf{x}) = \epsilon(\mathbf{x})^{-1} + \delta\kappa(\delta\mathbf{k}_2 \cdot x)\epsilon(\mathbf{x})^{-2}\sigma_2, \tag{5.1}$$

where

$$\epsilon(\mathbf{x}) = \begin{cases} 1 + J, & \text{if } \mathbf{x} \in \Omega_1, \\ 1, & \text{if } \mathbf{x} \in \Omega_2. \end{cases}$$

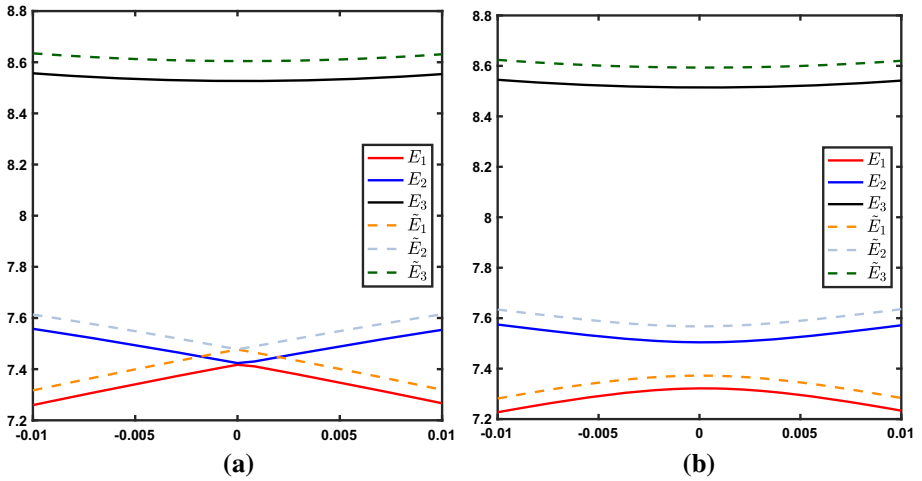

Fig. 7 Comparison of the unfitted Nitsche's method and the Fourier spectral method (solid line: the Unfitted Nitsche's method and dashed line: the Fourier spectral method): **a** $J = 2$ and $\gamma = 0$; **b** $J = 2$ and $\gamma = 0.1$

In (5.1), δ is a constant. It is chosen such that the coefficient matrix W is positive definite. The function $\kappa(\cdot)$ is the transition function (domain wall function) (2.11).

5.2.1 Verification of Accuracy

In this part, we conduct a benchmark numerical study to verify the optimal convergence of the unfitted Nitsche's method (3.52). Similarly, the convergence rate is approximated by the following relative errors

$$\hat{e}_i = \frac{|E_{i,h_j}(k_\parallel) - E_{i,h_{j+1}}(k_\parallel)|}{E_{i,h_{j+1}}(k_\parallel)}.$$

In this test, we take $k_\parallel = 0.56\pi$, $\delta = 0.1$ and $L = 10$. We focus on the computation of the first six eigenvalues. The numerical results of the convergence test are summarized in Fig. 8 for $J = 2$ and $J = 10$. From the data in Fig. 8, it is evident that the numerical eigenvalues computed by the unfitted Nitsche's method (3.52) converges at the optimal rate $\mathcal{O}(h^2)$. This is consistent with the theoretical result in the Theorem 6.

5.2.2 Computation of the Topological Edge Modes

In this paper, we provide numerical examples to demonstrate that the proposed unfitted Nitsche's method is an efficient method to compute the topological edge modes in the heterogeneous setting.

Test case 1 First of all, we consider the computation of the topological edge states with small jump ratio. In this test, we choose $J = 2$, $\delta = 0.6$ and $L = 80$. In Fig. 9a, we show the plot of first 85 eigencurves in term of $k_\parallel$. In Fig. 9a, we can see that the red eigencurve is separated from the eigencurves, which indicates edge states. To demonstrate the existence of edge states, we sketch the modulus of the 79th, 80th, and 81th eigenfunctions at the point $k_\parallel = \frac{2\pi}{3}$ in Fig. 10. What stands out in the table is that the 81th eigenfunction is located at the center of the computational domain but the 79th and 80th are both located the boundary

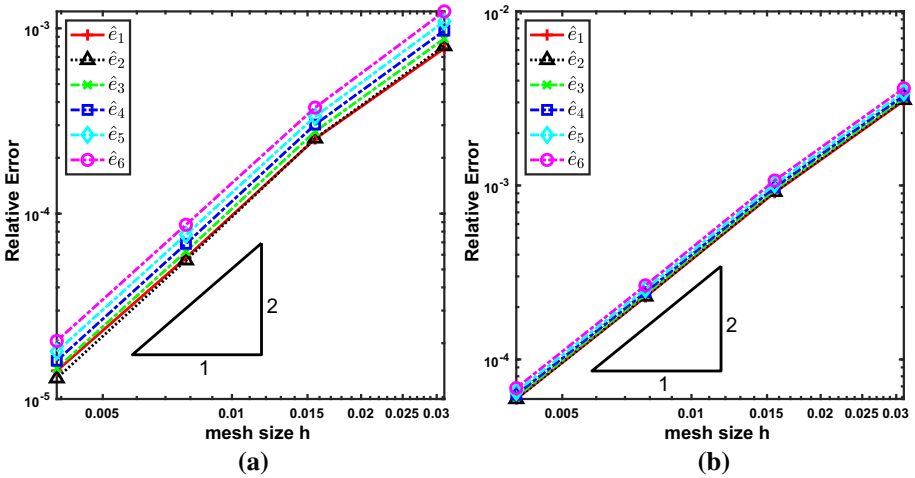

Fig. 8 Numerical errors for eigenvalue approximation: **a** $J = 2$ and $\delta = 0.1$; **b** $J = 10$ and $\delta = 0.1$

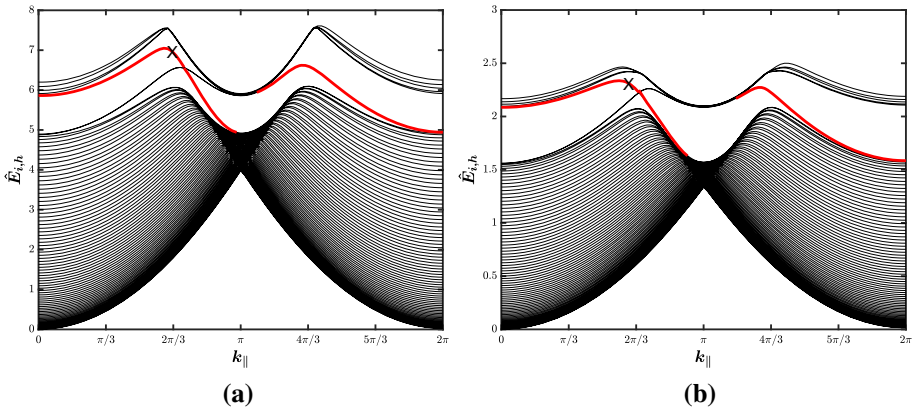

Fig. 9 Plot of the first 85 eigencurves for with $L = 80$ where the edge mode is corresponding to the line mark by 'X': **a** Case $J = 2$ and $\delta = 0.6$; **b** Case $J = 10$ and $\delta = 0.7$

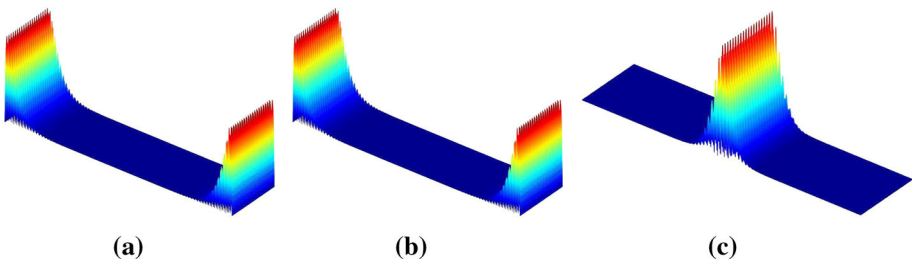

Fig. 10 Plot of the module of the eigenfunctions: **a** The 79th eigenfunction; **b** The 80th eigenfunction; **c** The 81th eigenfunction

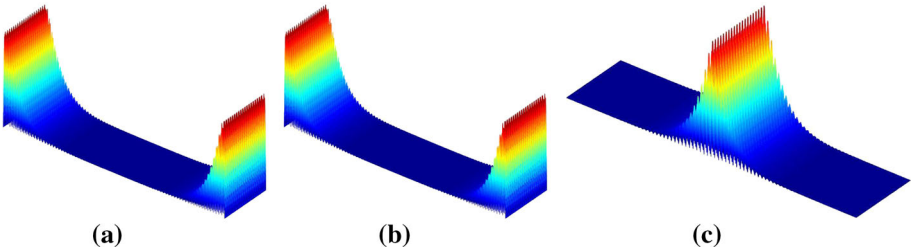

Fig. 11 Plot of the module of the eigenfunctions: **a** The 79th eigenfunction; **b** The 80th eigenfunction; **c** The 81th eigenfunction

of the computational domain. It suggests that the 81th eigenfunction is the true edge state of eigenvalue problem (2.12)–(2.14). The other two are referred as to pseudo edge state which appear due to fact that the artificial truncation of the computational domain creates two other edges.

Test case 2. We consider a relative large jump ratio here. In this test, we choose $J = 10$, $\delta = 0.7$ and $L = 80$. The plots of eigencurves are presented in Fig. 9b. Similarly, we list the plots of the modules of the 79th, 80th, and 81th eigenfunctions at the point $k_{\|} = \frac{2\pi}{3}$ in Fig. 11. We observe the same phenomena as in **Test case 1**. In particular, we can observe the existence of edge mode.

6 Conclusion

In this paper, we propose new unfitted Nitsche's methods based on the Floquet-Bloch transform for efficiently simulating photonic graphene with heterogeneous structure. By taking advantage of the structure of underlying meshes, we establish a sharp trace inequality for cut elements, which is the key ingredient to show the stability of the Nitsche's bilinear forms. The theoretical foundation of the proposed methods builds upon the abstract spectral approximation theory by Babuška and Osborn. The performance of the proposed unfitted methods is tested with a series of benchmark numerical examples. Numerical comparison with the Fourier spectral method suggests our method is a better choice for simulating topological materials with discontinuous material weights. Generalization of the proposed method to other domains has no numerical difficulties in designing algorithms, but the uniform analysis for general domains requires techniques beyond the scope of this paper. Thus we shall leave it as a future work. In future, we also plan to combine the superconvergent tool for unfitted Nitsche's method in [14] to further improve the accuracy and reduce the CPU time. Moreover, we will apply the results in this work to simulate the evolution of these novel wave modes [21,44].

Acknowledgements The authors thank Professor Michael I. Weinstein for useful discussions. H.G. was partially supported by Andrew Sisson Fund of the University of Melbourne, X.Y. was partially supported by the NSF grant DMS-1818592, and Y.Z. was partially supported by NSFC grant 11871299.

Author Contributions All authors make equal contributions to this manuscript.

Funding Hailong Guo was partially supported by Andrew Sisson Fund of the University of Melbourne. Xu Yang was partially supported by the NSF grant DMS-1818592. Yi Zhu was partially supported by NSFC grant 11871299.

Data Availability The authors affirm that this manuscript submitted to Journal of Scientific Computing is an honest, accurate, and transparent account of the study being reported; The data was generated by the authors using the numerical schemes proposed in this manuscript. Data will be available on reasonable requests.
Code Availability All codes were written by the authors and will be available on reasonable requests.

Declarations

Conflict of interest The authors declare that they have not known competing financial interests or personal relationships that could have appeared to influence the work reported in this paper.

A Proof of the Lemma 2

A.1 A Technical Lemma

Before giving the proof of Lemma 2, we present a lemma that we shall use.

Lemma 5 *Let* $\mathbf{x}^j = (x_1^j, x_2^j)$, $j = 1, 2, 3$, *be the three vertices triangle* K *and* $b_j(\mathbf{x})$ *be the standard nodal basis function associated with* $\mathbf{x}^j$. *Then the following relationship holds*

$$|b_j(\mathbf{x})| \le 2h|\nabla b_j|, \quad \forall \mathbf{x} \in K, \tag{A.1}$$

for $j = 1, 2, 3$.

Proof Without loss of generality, we only prove (A.1) for $j = 1$. Using the area coordinates [10], we have

$$b_1(\mathbf{x}) = \frac{(x_2 - x_2^3)(x_1^3 - x_1^2) - (x_1 - x_1^2)(x_2^3 - x_2^2)}{2|K|}, \tag{A.2}$$

and

$$\nabla b_i = \left(\frac{-(x_2^3 - x_2^2)}{2|K|}, \frac{(x_1^3 - x_1^2)}{2|K|} \right). \tag{A.3}$$

From the above two expressions, we can deduce that

$$|b_i(\mathbf{x})| \le h \frac{|x_1^3 - x_1^2| + |(x_2^3 - x_2^2)|}{2|K|} \le 2h \frac{\sqrt{|x_1^3 - x_1^2|^2 + |(x_2^3 - x_2^2)|^2}}{2|K|} = 2h|\nabla b_i|$$

where we have used the fact $|(x_2 - x_2^3| \le h$ and $|x_1 - x_1^2| \le h$ for any point $\mathbf{x} = (x_1, x_2)$ in the triangle K. □

A.2 Proof of Lemma 2

It is sufficient to show the lemma for the basis functions b_j since ϕ_h is a linear combination of b_j. Using Lemma 5, we can deduce that

$$\|b_j\|_{0,\Gamma_T}^2 \le |\Gamma_T| \|b_j\|_{0,\infty,\Gamma_T}^2 \le |\Gamma_T| \|b_j\|_{0,\infty,K_i}^2 \le 4h^2 |\Gamma_T| |\nabla b_i|^2 = \frac{4h^2|\Gamma_T|}{|K_i|} \|\nabla b_i\|_{0,K_i}^2;$$

which completes the proof of (3.24). The inequality (3.25) is implied in the above proof.

References

1. Ablowitz, M.J., Nixon, S.D., Zhu, Y.: Conical diffraction in honeycomb lattices. Phys. Rev. A **79**, 053830 (2009)
2. Ablowitz, M.J., Zhu, Y.: Nonlinear waves in shallow honeycomb lattices. SIAM J. Appl. Math. **72**, 240–260 (2012)
3. Ablowitz, M.J., Zhu, Y.: Nonlinear wave packets in deformed honeycomb lattices. SIAM J. Appl. Math. **73**, 1959–1979 (2013)
4. Annavarapu, C., Hautefeuille, M., Dolbow, J.E.: A robust Nitsche's formulation for interface problems. Comput. Methods Appl. Mech. Eng. **225**(228), 44–54 (2012)
5. Babuška, I.: The finite element method for elliptic equations with discontinuous coefficients. Computing (Arch. Elektron. Rechnen) **5**, 207–213 (1970)
6. Babuška, I., Osborn, J.: Eigenvalue Problems. Handbook of Numerical Analysis, vol. II, pp. 641–787. North-Holland, Amsterdam (1991)
7. Boffi, D.: Finite element approximation of eigenvalue problems. Acta Numer. **19**, 1–120 (2010)
8. Burman, E., Claus, S., Hansbo, P., Larson, M.G., Massing, A.: CutFEM: discretizing geometry and partial differential equations. Int. J. Numer. Methods Eng. **104**, 472–501 (2015)
9. Chen, Z., Zou, J.: Finite element methods and their convergence for elliptic and parabolic interface problems. Numer. Math. **79**, 175–202 (1998)
10. Ciarlet, P.G.: The Finite Element Method for Elliptic Problems. Classics in Applied Mathematics, vol. 40. Society for Industrial and Applied Mathematics (SIAM), Philadelphia (2002). Reprint of the 1978 original [North-Holland, Amsterdam; MR0520174 (58 #25001)]
11. Drouot, A., Weinstein, M.: Edge states and the valley Hall effect. Adv. Math. **368**, 107142 (2020)
12. Guo, H., Yang, X.: Gradient recovery for elliptic interface problem: II. Immersed finite element methods. J. Comput. Phys. **338**, 606–619 (2017)
13. Guo, H., Yang, X.: Gradient recovery for elliptic interface problem: I. Body-fitted mesh. Commun. Comput. Phys. **23**, 1488–1511 (2018)
14. Guo, H., Yang, X.: Gradient recovery for elliptic interface problem: III. Nitsche's method. J. Comput. Phys. **356**, 46–63 (2018)
15. Guo, H., Yang, X., Zhang, Z.: Superconvergence of partially penalized immersed finite element methods. IMA J. Numer. Anal. **38**, 2123–2144 (2018)
16. Guo, H., Yang, X., Zhu, Y.: Bloch theory-based gradient recovery method for computing topological edge modes in photonic graphene. J. Comput. Phys. **379**, 403–420 (2019)
17. Haldane, F.D.M., Raghu, S.: Possible realization of directional optical waveguides in photonic crystals with broken time-reversal symmetry. Phys. Rev. Lett. **100**, 013904 (2008)
18. Hansbo, A., Hansbo, P.: An unfitted finite element method, based on Nitsche's method, for elliptic interface problems. Comput. Methods Appl. Mech. Eng. **191**, 5537–5552 (2002)
19. Hou, S., Liu, X.-D.: A numerical method for solving variable coefficient elliptic equation with interfaces. J. Comput. Phys. **202**, 411–445 (2005)
20. Hou, S., Song, P., Wang, L., Zhao, H.: A weak formulation for solving elliptic interface problems without body fitted grid. J. Comput. Phys. **249**, 80–95 (2013)
21. Hu, P., Hong, L., Zhu, Y.: Linear and nonlinear electromagnetic waves in modulated honeycomb media. Stud. Appl. Math. **144**, 18–45 (2020)
22. Kellogg, R.B.: On the Poisson equation with intersecting interfaces. Appl. Anal. **4**, 101–129. Collection of articles dedicated to Nikolai Ivanovich Muskhelishvili (1974/75)
23. Khanikaev, A.B., Mousavi, S.H., Tse, W.-K., Kargarian, M., MacDonald, A.H., Shvets, G.: Photonic topological insulators. Nat. Mater. **12**, 233–239 (2013)
24. Lee-Thorp, J.P., Weinstein, M.I., Zhu, Y.: Elliptic operators with honeycomb symmetry: Dirac points, edge states and applications to photonic graphene. Arch. Ration. Mech. Anal. **232**, 1–63 (2019)
25. LeVeque, R.J., Li, Z.: The immersed interface method for elliptic equations with discontinuous coefficients and singular sources. SIAM J. Numer. Anal. **31**, 1019–1044 (1994)
26. Li, Z.: The immersed interface method using a finite element formulation. Appl. Numer. Math. **27**, 253–267 (1998)
27. Li, Z., Ito, K.: The Immersed Interface Method. Frontiers in Applied Mathematics, vol. 33. Society for Industrial and Applied Mathematics (SIAM), Philadelphia. Numerical solutions of PDEs involving interfaces and irregular domains (2006)
28. Li, Z., Lin, T., Wu, X.: New Cartesian grid methods for interface problems using the finite element formulation. Numer. Math. **96**, 61–98 (2003)
29. Lin, T., Lin, Y., Zhang, X.: Partially penalized immersed finite element methods for elliptic interface problems. SIAM J. Numer. Anal. **53**, 1121–1144 (2015)

30. Lu, J., Marzuola, J.L., Watson, A.B.: Defect resonances of truncated crystal structures. arXiv preprint arXiv:2006.07762 (2020)
31. Lu, L., Joannopoulos, J.D., Soljačić, M.: Topological photonics. Nat. Photonics **8**, 821–829 (2014)
32. Mousavi, S.H., Khanikaev, A.B., Wang, Z.: Topologically protected elastic waves in phononic metamaterials. Nat. Commun. **6**, 1–7 (2015)
33. Nitsche, J.: *über ein Variationsprinzip zur Lösung von Dirichlet-Problemen bei Verwendung von Teilräumen, die keinen Randbedingungen unterworfen sind*. Abh. Math. Sem. Univ. Hamburg **36**, 9–15. Collection of articles dedicated to Lothar Collatz on his sixtieth birthday (1971)
34. Peskin, C.S.: Numerical analysis of blood flow in the heart. J. Comput. Phys. **25**, 220–252 (1977)
35. Peskin, C.S.: The immersed boundary method. Acta Numer. **11**, 479–517 (2002)
36. Plotnik, Y., Rechtsman, M.C., Song, D., Heinrich, M., Zeuner, J.M., Nolte, S., Lumer, Y., Malkova, N., Xu, J., Szameit, A., Chen, Z., Segev, M.: Observation of unconventional edge states in 'photonic graphene'. Nat. Mater. **13**, 57–62 (2014)
37. Rechtsman, M.C., Zeuner, J.M., Plotnik, Y., Lumer, Y., Podolsky, D., Dreisow, F., Nolte, S., Segev, M., Szameit, A.: Photonic floquet topological insulators. Nature **496**, 196–200 (2013)
38. Skorobogatiy, M., Yang, J.: Fundamentals of Photonic Crystal Guiding. Cambridge University Press, Cambridge (2009)
39. Süsstrunk, R., Huber, S.D.: Observation of phononic helical edge states in a mechanical "topological insulator". Science **349**, 47–50 (2015)
40. Thicke, K., Watson, A.B., Lu, J.: Computing edge states without hard truncation. SIAM J. Sci. Comput. **43**(2), B323–B353 (2021)
41. Trefethen, L.N.: Spectral Methods in MATLAB. SIAM, Philadelphia (2000)
42. Wang, L., Zheng, H., Lu, X., Shi, L.: A Petrov–Galerkin finite element interface method for interface problems with Bloch-periodic boundary conditions and its application in phononic crystals. J. Comput. Phys. **393**, 117–138 (2019)
43. Xiao, M., Ma, G., Yang, Z., Sheng, P., Zhang, Z.Q., Chan, C.T.: Geometric phase and band inversion in periodic acoustic systems. Nat. Phys. **11**, 240–244 (2015)
44. Xie, P., Zhu, Y.: Wave packet dynamics in slowly modulated photonic graphene. J. Differ. Equ. **267**, 5775–5808 (2019)